

DEPARTMENT OF ELECTRONIC SYSTEMS

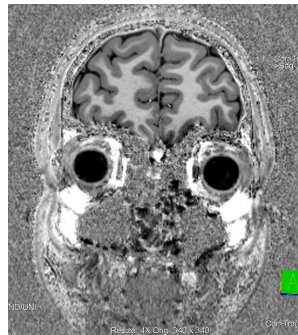


TFE4940 - ELECTRONIC SYSTEMS DESIGN AND INNOVATION,  
MASTER'S THESIS

---

# Measuring RF-Induced Heating of a Phantom with PRF Shift Thermometry

---



*Author:*  
Carl Fredrik Haakonon

*Supervisor:* Pierluigi Salvo Rossi  
*Co-Supervisor:* Pål Erik Goa

June, 2022

# Abstract

During an MRI scan, the Specific Absorption Rate (SAR) is simulated to ensure the heating due to the imaging sequence's Radio Frequency (RF) pulses does not exceed the regulatory limits. Verifying the simulations by measuring the actual heating in phantoms with simple geometry is therefore important. One method of measuring temperature change is PRF shift thermometry, which consists of acquiring phase images and converting them to temperature maps. This master's thesis investigates whether PRF shift thermometry at 7T, combined with a temperature probe for 0th and 1st order magnetic field drift correction, is accurate enough to measure the RF-induced heating of a phantom due to the thermometry imaging sequence itself. A custom GRE sequence with an adjustable heating pulse was made so the sequence SAR could be adjusted without changing the imaging parameters. Series of 77 phase images were acquired sequentially for 10 minutes with the custom sequence to measure the temperature change induced by the imaging sequence. A custom spherical agar phantom was used for the experiments. The series of phase images were converted to temperature maps, and the 0th and 1st order spatial drift was corrected using a temperature probe. The resulting temperature maps were evaluated. The accuracy of the temperature maps acquired with the PRF shift thermometry method proposed in this report did not satisfy the predefined accuracy goal of  $0.1^{\circ}\text{C}$  at all spatial locations. At a temperature probe used for validation, the calculated Root Mean Square Error (RMSE) ranged from  $0.12^{\circ}\text{C}$  to  $0.37^{\circ}\text{C}$  for the 10 minutes series. The errors seemed to result from 2nd order spatial drift, which looked reproducible and may therefore be possible to remove. Further experiments and work with the sequence and post-processing may improve the accuracy so that the method can be used for verification of SAR calculations in the future.

# Sammendrag

Under MR-avbildning simuleres den spesifikke absorpsjonsraten (SAR) for å sikre at oppvarmingen som følge av bildesekvensens radiofrekvenspulser (RF) ikke overskrider de regulatoriske grensene. Å verifisere simuleringene ved å måle selve oppvarmingen i fantomer med enkel geometri er derfor viktig. Én metode for å måle temperaturendringer er PRF-skiftermometri, som består av å ta fasebilder og konvertere dem til temperaturkart. Denne masteroppgaven undersøker om PRF-skiftermometri ved 7T, kombinert med en temperatursensor for 0. og 1. ordens magnetfeltdriftskorreksjon, er nøyaktig nok til å måle den RF-induserte oppvarmingen av et fantom som følge av bildesekvensen brukt til termometrien. En GRE-sekvens med justerbar varmpuls ble laget slik at sekvensens SAR kunne justeres uten å endre opptaksparameterne. Serier med 77 fasebilder ble tatt sekvensielt i løpet av 10 minutter for å måle temperaturendringen induisert av bildesekvensen selv. Et tilpasset sfærisk agarfantom ble brukt til eksperimentene. Serien av fasebilder ble konvertert til temperaturkart, og 0. og 1. ordens romlig drift ble korrigert ved hjelp av en temperatursensor. De resulterende temperaturkartene ble evaluert. Nøyaktigheten til temperaturkartene oppnådd med PRF-skiftermometri, som presentert i denne rapporten, tilfredstilte ikke det forhåndsdefinerte nøyaktighetsmålet på  $0,1^{\circ}\text{C}$  i hele bildet. Ved temperatursensoren som ble brukt til validering varierte den beregnede RMSE verdien fra  $0,12^{\circ}\text{C}$  til  $0,37^{\circ}\text{C}$  for de 10 minutter lange seriene. Feilene så ut til å skyldes romlig drift av 2. orden, som virket reproducerbar og derfor kanskje mulig å fjerne. Ytterligere eksperimenter og arbeid med sekvensen og post-prosessering kan mulig forbedre nøyaktigheten slik at metoden kan brukes til verifikasjon av SAR-beregninger i fremtiden.

# Acknowledgments

I would like to express my gratitude to my supervisor Pål Erik Goa. Thank you for all your help and guidance. This project would not have been possible without you and the hours you have invested in it. I am proud to say that we finally managed to produce a simple spherical phantom. I would also like to thank Maria Tunset Grinde who helped me cook the agar phantom and took incredible images of me in a lab coat where I looked super smart. Lastly, I wish to show my appreciation to Neil Peter Jerome. Without your help, I would still work on the sequence programming.

# Contents

<b>Abstract</b> . . . . .	<b>i</b>
<b>Sammendrag</b> . . . . .	<b>ii</b>
<b>Acknowledgments</b> . . . . .	<b>iii</b>
<b>Contents</b> . . . . .	<b>iv</b>
<b>Figures</b> . . . . .	<b>vi</b>
<b>Tables</b> . . . . .	<b>viii</b>
<b>Acronyms</b> . . . . .	<b>ix</b>
<b>1 Introduction</b> . . . . .	<b>1</b>
1.1 Background . . . . .	1
1.2 Motivation and Problem Description . . . . .	2
1.3 Aim . . . . .	3
1.4 Outline . . . . .	3
<b>2 MR Basics and the GRE Sequence</b> . . . . .	<b>4</b>
2.1 Spins, Precession and Net Magnetization . . . . .	4
2.2 Excitation and Relaxation . . . . .	6
2.3 Image Formation . . . . .	7
2.4 The Gradient Recalled Echo Sequence . . . . .	9
2.5 Dual echo sequence . . . . .	13
2.6 SAR . . . . .	14
2.7 Ultra-High Field MR . . . . .	15
<b>3 PRF Shift Thermometry</b> . . . . .	<b>17</b>
3.1 Field Inhomogeneity and Phase . . . . .	17
3.2 Chemical Shift of Water Protons . . . . .	18
3.3 Measuring Temperature . . . . .	20
3.4 Magnet Design and Shimming . . . . .	21
3.5 Magnetic Field Drift . . . . .	24
3.6 Related work . . . . .	25
<b>4 Method</b> . . . . .	<b>27</b>
4.1 Setup . . . . .	27
4.2 Custom Phantom . . . . .	30
4.3 Custom GRE Sequence With Adjustable SAR . . . . .	32
4.4 Sequence Setup Parameters . . . . .	33
4.5 Temperature Map Formation Pipeline . . . . .	35
4.6 0th Order Spatial Drift Correction . . . . .	38

4.7	1st Order Spatial Drift Correction . . . . .	39
4.8	Experiments . . . . .	45
4.9	Evaluation of the Temperature Maps . . . . .	46
<b>5</b>	<b>Results . . . . .</b>	<b>48</b>
5.1	Session Temperatures . . . . .	48
5.2	Drift Correction . . . . .	50
5.3	Temperature Map Evaluation . . . . .	54
5.4	Oscillating Temperature . . . . .	57
<b>6</b>	<b>Discussion . . . . .</b>	<b>58</b>
6.1	Session Temperatures and the Probe's Reliability . . . . .	58
6.2	Gradient System Temperatures and Reproducibility . . . . .	59
6.3	Temperature Maps and Drift Correction . . . . .	60
6.4	Performance . . . . .	61
6.5	Oscillating Temperature . . . . .	62
<b>7</b>	<b>Conclusion and Future Work . . . . .</b>	<b>63</b>
7.1	Conclusion . . . . .	63
7.2	Future Work . . . . .	64
	<b>Bibliography . . . . .</b>	<b>65</b>
<b>A</b>	<b>Additional Results . . . . .</b>	<b>68</b>
<b>B</b>	<b>Temperature Experiments . . . . .</b>	<b>72</b>
B.1	Fiber Optic Temperature Probe Validation . . . . .	72
B.2	Agar Temperature Experiment . . . . .	74
<b>C</b>	<b>Code . . . . .</b>	<b>77</b>
C.1	Temperature Map Formation . . . . .	77
C.2	0th Order Drift Correction . . . . .	78
C.3	1st Order Drift Correction . . . . .	79

# Figures

2.1	The main magnetic field $B_0$ in an MR scanner. . . . .	4
2.2	Spin distribution and net magnetization. . . . .	5
2.3	RF pulse produced by a transmit coil . . . . .	6
2.4	Net magnetization precessing at the Larmor frequency . . . . .	7
2.5	Gradient . . . . .	8
2.6	Gradient recalled echo sequence diagram . . . . .	10
2.7	Slice selection . . . . .	11
2.8	K-space scanning . . . . .	12
2.9	Magnitude and phase image . . . . .	13
2.10	Simulation of 10g averaged SAR . . . . .	15
3.1	The shielding effect . . . . .	18
3.2	Hydrogen bonding of water molecules . . . . .	19
3.3	Temperature map of a phantom . . . . .	21
3.4	Magnet design and coils . . . . .	22
3.5	Concept of shimming . . . . .	22
3.6	Shimming . . . . .	23
3.7	Decomposed field drift. . . . .	24
4.1	Siemens MAGNETOM Terra and head coil. . . . .	28
4.2	Phantom and temperature probes placed in the coil. . . . .	29
4.3	Orientation and placement of the phantom and temperature probes. . . . .	29
4.4	Localizer images of the agar phantom. . . . .	30
4.5	Agar phantom . . . . .	30
4.6	Phantom cooking process . . . . .	32
4.7	Gradient recalled echo sequence with tunable SAR . . . . .	33
4.8	A series of images . . . . .	35
4.9	Sequence of phase images from one slice . . . . .	35
4.10	Temperature map formation . . . . .	36
4.11	Sequence of temperature images from one slice . . . . .	37
4.12	0th order drift estimation. . . . .	38
4.13	Subtraction of 0th order drift . . . . .	39
4.14	Sinogram produced from a mean temperature map . . . . .	40
4.15	Estimation of projection gradient . . . . .	41

4.16	Finding the angle of projection with maximum slope . . . . .	41
4.17	Producing a 1D image of the gradient from 2D image. . . . .	42
4.18	Estimation of 1st order drift . . . . .	43
4.19	Making 1st order drift estimate map . . . . .	44
4.20	Subtraction of 1st order drift . . . . .	45
5.1	Session temperature data . . . . .	49
5.2	Mean gradient system temperatures during and in-between acquisitions . . . . .	50
5.3	Raw temperature maps from Run 1 . . . . .	51
5.4	0th order drift corrected temperature maps from Run 1 . . . . .	53
5.5	0th and 1st order drift corrected images from Run 1 . . . . .	54
5.6	ROI temperatures from 1: <i>Standard series with low SAR</i> (slice 2, Run 1) plotted with the probe data . . . . .	55
5.7	ROI temperatures from 3: <i>Standard series with high SAR</i> (slice 2, Run 1) plotted with the probe data . . . . .	55
5.8	ROI temperatures from 1: <i>Standard series with low SAR</i> (slice 2, Run 2) plotted with the probe data . . . . .	56
5.9	ROI temperatures from 3: <i>Standard series with high SAR</i> (slice 2, Run 2) plotted with the probe data . . . . .	56
5.10	Oscillating drift in high SAR series . . . . .	57
A.1	Raw temperature maps from Run 2 . . . . .	69
A.2	0th order drift corrected temperature maps from Run 2 . . . . .	70
A.3	0th and 1st order drift corrected images from Run 2 . . . . .	71
B.1	Temperature probe test . . . . .	73
B.2	Agar temperature experiment setup . . . . .	75
B.3	Temperature plot from agar gel experiment . . . . .	75



# Tables

4.1	Phantom ingredients. . . . .	31
4.2	Standard sequence parameters. . . . .	34
4.3	Slice y-positions relative to the isocenter . . . . .	35
5.1	Estimated 0th order spatial drift for each series in Run 1 . . . . .	52
5.2	Estimated 0th order spatial drift for each series in Run 2 . . . . .	52
5.3	Estimated gradient slopes due to 1st order spatial drift . . . . .	54
5.4	RMSE values . . . . .	57

# Acronyms

**ADC** Analogue Digital Converter. 9, 10

**FA** Flip Angle. 6, 15, 32

**GRE** Gradient Recalled Echo. 2, 4, 9–11, 23, 25, 32, 33, 63

**HIFU** High-Intensity Focused Ultrasound. 2

**MR** Magnetic Resonance. vi, 1–4, 7–9, 11, 15–18, 22, 25–28, 32, 72, 74

**MRI** Magnetic Resonance Imaging. 1, 2, 4, 9, 14, 28, 63

**PRF** Proton Resonance Frequency. 2–5, 17–21, 25–27, 59, 61, 63, 64

**pTx** Parallel Transmission. 16

**RF** Radio Frequency. 1–3, 6–11, 14, 15, 22, 25, 27, 30, 32, 33, 46, 50, 58, 62–64

**RMSE** Root Mean Square Error. viii, 46, 47, 55–57, 61–64

**ROI** Region of Interest. vii, 25, 38, 46, 47, 54–57, 61–63

**SAR** Specific Absorption Rate. vii, 2, 14–16, 25, 32, 33, 46, 54–64

**SNR** Signal to Noise Ratio. 1, 15

**TE** Echo Time. 12

**TR** Repetition Time. 7, 11–13, 34, 62

**UHF** Ultra High Field. 1, 15, 16

# Chapter 1

## Introduction

### 1.1 Background

Magnetic Resonance Imaging (MRI) is one of the most common medical imaging modalities used clinically in developed countries. Due to its excellent ability to image soft tissues, it can be used to investigate tumors, stroke, dementia, infection, and for many other diseases and research areas. MRI does not use ionizing radiation, contrary to modalities like X-ray, CT, and PET. It is therefore considered 100% safe to use, as the only side effect is heating. MRI uses electromagnetic pulses at Radio Frequency (RF), just like your mobile phone, computer or radio.

It was Paul C. Lauterbur who in 1973 first introduced the world to the concept of MRI in his paper *Image Formation by Induced Local Interactions: Examples Employing Nuclear Magnetic Resonance*[1]. The paper described how a nuclei placed in a strong magnetic field  $B_0$  will precess, and that the nuclei can be excited by on-resonance RF pulses. The excited nuclei can then be spatially encoded by gradients, and an image could be formed from the RF signal emitted back from the nuclei.

The strength of the main magnetic field  $B_0$  determines the precessional frequency of the nuclei, and therefore affects the image acquisition and results. A higher  $B_0$  is linked to an increased Signal to Noise Ratio (SNR) and contrast, and can also reduce scan times. Due to these advantages, the field strength of MR scanners have increased since its beginning in the seventies. In 2022, 1.5T and 3T are the most common field strengths used clinically, but higher field strengths are increasingly common. Trending today is Ultra High Field (UHF) MRI, defined as  $B_0 \geq 7T$ .

Although high main field strength  $B_0$  has its advantages, there are negative sides too. Among those are more and increasingly inhomogeneous heating. The frequency of the RF pulses must match the precessional frequency of the nuclei, which increases with  $B_0$ . Thus, higher frequency RF are used, meaning more energy and shorter wavelength. If the wavelength of the RF pulse is short enough to be comparable to the imaged object's size, standing waves can occur. Local hot spots can then arise, i.e. inhomogeneous heating.

The temperature increase in MR needs to be monitored to ensure the safety, as too much heating can be harmful. As it is not possible to measure the heating while performing a regular MRI scan, the Specific Absorption Rate (SAR) is simulated and restricted. SAR is a measure of absorbed energy by a given volume of tissue (W/kg). The International Electrotechnical Commission (IEC) have defined a set of regulatory limits for the SAR to ensure the temperature increase is within safe limits. In addition, the maximum temperature increase is restricted to 1°C. The SAR is simulated before each new scan, and if the sequence does not satisfy all regulatory limits, it must be modified until it does. This way the safety of the imaged subject is ensured.

## 1.2 Motivation and Problem Description

As simulations of the SAR are used to verify the safety of MRI sequence, it is important to know that the simulations are accurate and reliable. To do so, the simulated SAR is verified against the actual temperature increase. This is done at simple geometry phantoms, as for example a spherical phantom.

Verification of the simulations, as described above, requires a method for measuring the actual temperature change. While this could be done by using multiple MR compatible temperature probes to measure the RF-induced heating of an applied sequence, the probes will not yield full spatial information. Alternatively, temperature images acquired with MR thermometry could be used to measure the RF-induced heating due to the thermometry imaging sequence itself. Simulations could then be run on the thermometry sequence, and verified by the temperature maps produced by it. This could make it easier to validate the safety of new transmit coils for use in MR.

A common MR thermometry method is Proton Resonance Frequency (PRF) shift thermometry. The method acquires phase images using a Gradient Recalled Echo (GRE) sequence, which can be converted to temperature maps. For example, PRF shift thermometry has previously been used to monitor the temperature in High-Intensity Focused Ultrasound (HIFU) treatment[2] and investigating implant safety[3].

The main challenge with PRF shift thermometry is magnetic field drift, which is small changes/drifts in the main field  $B_0$ . The drift can lead to large errors in the temperature estimates, and needs to be corrected for. When used along with for example HIFU, areas of approximately zero temperature change can be used for drift correction, as the observed temperature change in these regions will be due to drift. The most common way of correcting for field drift in PRF shift thermometry is by estimating and subtracting the drift based on measurements of unheated areas.

This would however however not be possible when measuring the RF induced heating of a phantom, as the entire phantom is heated. The RF induced heating is also relatively small (maximum 1°C), meaning a good accuracy is important. Correcting for the magnetic field drift is then crucial.

### 1.3 Aim

The aim of this thesis is to investigate whether PRF shift thermometry at 7T is accurate enough to measure the RF-induced heating in a phantom due to the thermometry sequence itself, using a temperature probe for 0th and 1st order drift correction of the temperature maps.

For the method to be considered as good enough, the accuracy should be at least  $0.1^{\circ}\text{C}$  across the entire temperature maps. The target accuracy is based on two criteria. Firstly, the RF induced heating is restricted by safety limits to  $1^{\circ}\text{C}$  (first-level control mode), meaning the accuracy of the thermometry should be significantly better than  $1^{\circ}\text{C}$ . Secondly, hot spots can occur at 7T due to inhomogeneous heating, meaning the spatial information is important. Based on these criteria, the targeted accuracy was set to  $0.1^{\circ}\text{C}$  across the temperature maps.

### 1.4 Outline

The report is divided into seven chapters. Chapter 1 introduces the background and aim for the thesis. Following are two theoretical chapters. The first, Chapter 2, provides the basic Magnetic Resonance (MR) theory needed to understand PRF shift thermometry. The theory behind PRF shift thermometry is then presented in Chapter 3. Following, Chapter 4 shows how the theory was implemented and tested at a 7T scanner. The results are shown in Chapter 5, and discussed in Chapter 6. Finally, the conclusion and future work are presented in Chapter 7.

## Chapter 2

# MR Basics and the GRE Sequence

This chapter is a brief introduction to the fundamentals of MR imaging. Starting from the basic Magnetic Resonance (MR) physics, the chapter leads up to the Gradient Recalled Echo (GRE) sequence, which is central in PRF shift thermometry. The sections 2.1-2.5 are based on previous work by the author [4].

### 2.1 Spins, Precession and Net Magnetization

MRI signals originates mainly from  $^1H$  protons in water molecules. The protons can only produce the signal if placed in a strong external magnetic field. The main components of an MR scanner is therefore a superconductive coil that sets up a strong static main magnetic field  $B_0$ , as illustrated in Figure 2.1. Common field strengths on clinical scanners are 1,5T and 3T.

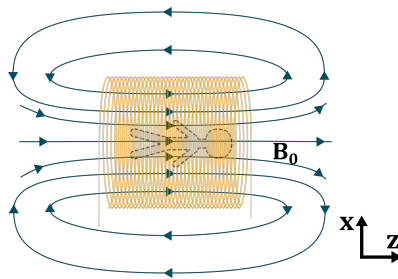


**Figure 2.1:** The main magnetic field  $B_0$  in an MR scanner.

Protons are spin- $\frac{1}{2}$  fermions, and have a small magnetic moment. The magnetic moment can be thought of as a tiny bar magnet. When placed in the strong field  $B_0$ , the spins are forced into two states. The magnetic moment can either align parallel (spin-up) or anti-parallel (spin-down) with  $B_0$ , where the latter is a higher energy state. The ratio of spins aligning parallel and anti-parallel is given by the Boltzmann distribution[5, p.65]. At room temperature, slightly more spins will be in the lower energy spin-up state.

In addition to aligning with  $B_0$ , the magnetic moments of the protons will precess. Due to the spin, the protons will experience a torque when placed in  $B_0$ . Similar to a spinning top with angular momentum in a gravitational field, the magnetic moment of the proton will precess around  $B_0$ . The precessional frequency, known as the Larmor frequency  $\omega_0$ , is given as

$$\omega_0 = \gamma B_0. \quad (2.1)$$

$B_0$  is the strength of the magnetic field [T], while  $\gamma$  is the gyromagnetic ratio [rad/s/T]. The gyromagnetic ratio is the ratio between the magnetic moment and the angular momentum of a particle or system. For a proton  $\gamma = 267.515 \cdot 10^8 \text{ rad/s/T}$ . The precessional frequency of a proton will be referred to as the Proton Resonance Frequency (PRF).

Figure 2.2a shows the parallel and anti-parallel spins precessing about  $B_0$ .

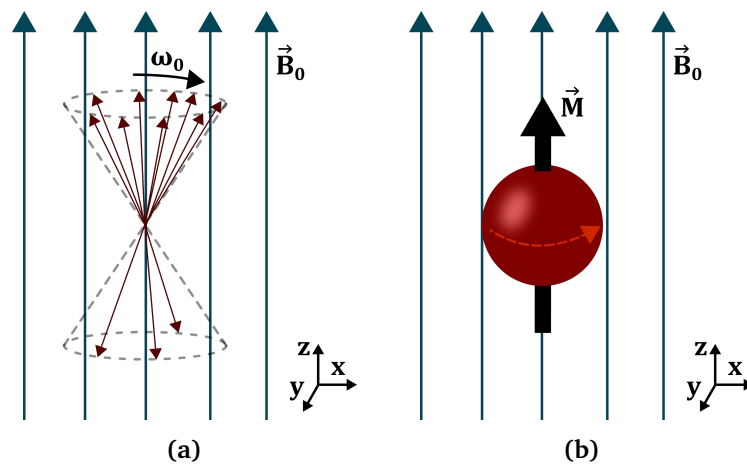


**Figure 2.2:** (a) Spins aligning either parallel or anti-parallel to the external field  $B_0$ . The spins precess with the Larmor frequency  $\omega_0$ . Each vector represents the magnetic moment of one proton. Slightly more protons will align parallel to the field. The ratio in the figure is exaggerated and not representative. (b) The spins within a small volume can be represented as a net magnetization, as shown in this figure. More spins are in the spin-up state. All the spins have random phase, cancelling out any transverse component. The net magnetization is therefore parallel to  $B_0$ .

To simplify calculations, the spins can be treated as a net magnetization vector with a net magnetic moment  $\vec{M}$ . The net magnetization describes the net contribution of all the protons within a small volume, and is illustrated in Figure 2.2b. By looking at the net effect of a large number of spins as a net magnetization, the magnetization vector can be described in classical terms by the Bloch equation[5, p.76-77].

## 2.2 Excitation and Relaxation

The net magnetization pointing along  $B_0$  does not produce a signal. To make a signal, Radio Frequency (RF) pulses are needed to rotate the net magnetization vector down towards the transverse x,y-plane. The net magnetization will then precess around  $B_0$ , and induce a signal in the receive coils.

The RF pulse is an oscillating magnetic field  $B_1$  produced by a transmit coil. The field oscillates on-resonance at the Larmor frequency, perpendicular to the main static field  $B_0$ . This is illustrated in Figure 2.3

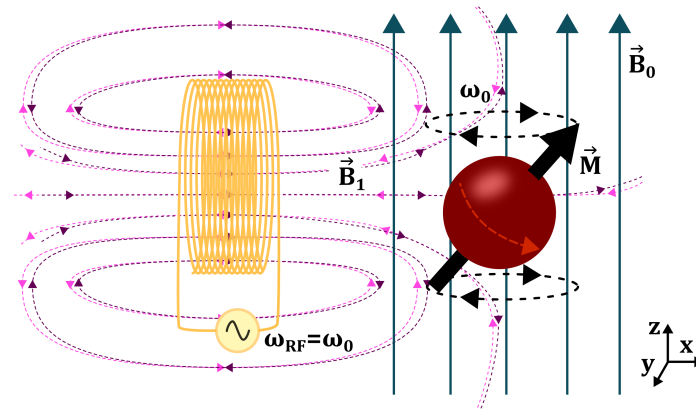


**Figure 2.3:** RF pulse produced by a transmit coil. The RF pulse is a magnetic field  $B_1$  produced by a coil with an oscillating current at  $\omega_{rf} = \omega_0$ .

When an RF pulse is applied perpendicular to  $B_0$ , the net magnetization is rotated towards the transverse x,y-plane. This is a result of protons in the spin-up state being flipped to spin-down, as well as moving in-phase. The net magnetization will then precess around  $B_0$  at  $\omega_0$ . This process is called RF excitation, and can be described mathematically by incorporating the expression of the RF pulse in the Bloch equation[5, p.77-80]. The angle of rotation from the z-axis is called the Flip Angle (FA). Figure 2.4 shows the net magnetization at two different FAs towards the transverse plane.



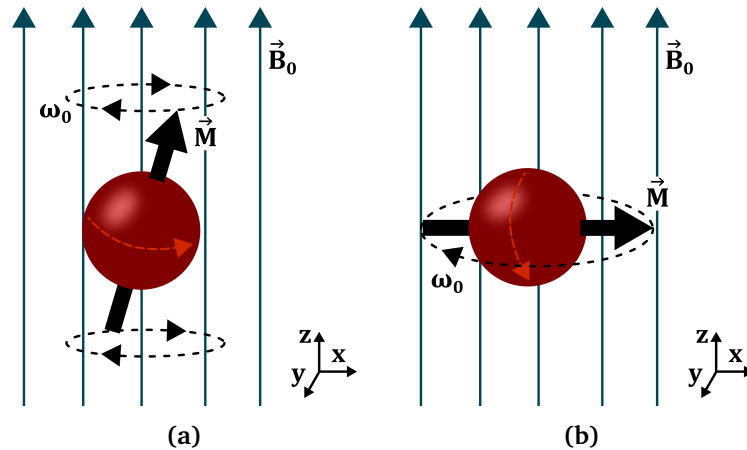


**Figure 2.4:** The net magnetization precessing at the Larmor frequency  $\omega_0$  at two different flip angles. The black arrow shows the net magnetic moment  $\vec{M}$ . (a) The net magnetization vector tipped  $\alpha$  degrees from the z-axis. (b) The net magnetization vector tipped  $90^\circ$  from the z-axis.

Once excited, the net magnetization induces a current in the receive coils. The current is produced by the time varying flux produced by the precession. The receive coils are placed perpendicular to  $B_0$ . For some setups the same coils are used for transmit and receive. See Figure 2.3. The measured signal is the transverse component of the net magnetization precessing at  $\omega_0$ .

When the RF pulse is turned off again, the net magnetization will start rotating back towards its equilibrium position. The equilibrium position is along  $B_0$  as shown in Figure 2.2b. The rotation back towards equilibrium is due to the opposite effects of excitation. The spins flipped during excitation are flipped back again, as well as all the spins gradually move out of phase again. The rate of longitudinal regrowth and dephasing is described by the parameters T1 and T2 respectively [5, p.91-94]. T1 and T2 are dependant on tissue and field strength. Using T1 and T2, the magnitude of the net magnetization's transverse component at position  $x$  at time  $t$  after excitation can be expressed as in Equation 2.2.

$$|M_{xy}(x, t)| = M_0(x) \left(1 - e^{-\frac{TR}{T1(x)}}\right) e^{-\frac{t}{T2^*(x)}} \quad (2.2)$$

$M_0$  is the equilibrium net magnetization, while TR is the repetition time of the sequence. TR is explained further in Section 2.4.

## 2.3 Image Formation

Excitation makes it possible to measure the MR signal, as the excited protons induce a current in the receive coils. If however  $B_0$  is the only present magnetic field, all the protons precess with the same frequency  $\omega$ . The signal is then of limited interest, as it holds no spatial information.

Spatial encoding is needed to make an image. In MR, the spatial encoding is achieved by using magnetic field gradients. The gradients are applied in x-, y- and z-direction. In this section, the principle of spatial encoding is illustrated using a single gradient in the x-direction only. Section 2.4 shows how gradients in all directions are used to form an image.

Gradient coils are used to produce the magnetic field gradients. Gradient coils are illustrated in in Figure 3.4b. With the gradient switched on, the field strength varies linearly along the gradients direction. Figure 2.5 shows the total magnetic field in the x-direction with the x-gradient  $G_x$  turned on. The same principle applies to the z and y directions.

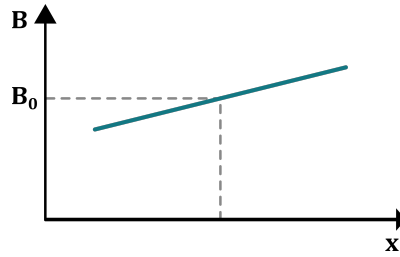


**Figure 2.5:** Gradient in the x-direction. The protons at position  $x$  will precess with a frequency given as  $\omega = \omega_0 + \gamma G_x x$ .

With the gradient in Figure 2.5 active, the protons will precess with a frequency

$$\omega(x) = \omega_0 + \gamma G_x x, \quad (2.3)$$

where  $\omega$  now depends on the spatial position  $x$ . This way the measured signal holds spatial information, making imaging possible. We will now look at how the image is produced from the signal measured in the receive coils.

Assume there is a various distribution of protons along the x-axis. They have been excited by an RF pulse and have a transverse component  $|M_{xy}(x, t)|$ , as described by Equation 2.2. After excitation, an x-gradient  $G_x$  is turned on. The protons will then precess with the frequency given in Equation 2.3. In addition to the gradient and main static field  $B_0$ , there will always be local inhomogeneities  $\Delta B(x)$ , resulting in a slight frequency offset  $\Delta\omega = \gamma\Delta B(x)$ . The signal from position  $x$  can then be expressed as

$$dS(x, t) = |M_{xy}(x, t)| e^{-i(\omega_0 t + \Delta\omega(x)t + \phi_0 + \gamma G_x x t)} dx, \quad (2.4)$$

where  $\phi_0$  is the initial phase of the proton relative to the receive coil. As all the precessing protons induce a small current in the receive coils, the total signal  $S(t)$  is an integral over  $x$ .

$$S(t) = \int |M_{xy}(x, t)| e^{-i(\omega_0 t + \Delta\omega(x)t + \phi_0 + \gamma G_x x t)} dx \quad (2.5)$$

By defining

$$k_x = \gamma G_x t, \quad (2.6)$$

Equation 2.5 can be rewritten as in Equation 2.7.

$$S(k_x, t) = \int |M_{xy}(x, t)| e^{-i\omega_0 t + \Delta\omega(x)t + \phi_0} e^{-ik_x x} dx \quad (2.7)$$

Equation 2.7 reveals that the measured signal is the spatial Fourier transform of the signal produced from all x-positions. This implies that the inverse Fourier transform yields the signal at all positions at time  $t$  after excitation.

$$\mathcal{F}^{-1}\{S(k_x, t)\} = S(x, t) = |M_{xy}(x, t)| e^{-i(\omega_0 t + \Delta\omega(x)t + \phi_0)} \quad (2.8)$$

Equation 2.8 can be seen as an 1D image of the x-axis. As shown in the equation, the image has both a magnitude and a phase value. These values can be used separately to produce a magnitude image and a phase image, which are illustrated in Figure 2.9 in Section 2.4.

As can be seen in Equation 2.8,  $G_x$  disappears in the inverse Fourier transform. This is the essence of MR imaging. Gradients are used to spatially encode the protons, and the signal is measured in k-space. An image is then produced by applying the inverse Fourier transform of the sampled k-space data. In the above example, a one dimensional image of the x-axis is produced. How a sequence is used to acquire 2D images is the theme of Section 2.4.

The signal produced is a high frequency signal at  $\approx \omega_0$ , which is approximately 300MHz at a 7T scanner. The high frequency carrier frequency is removed with demodulation[5, p.97-100]. In demodulation, the signal is multiplied with a reference signal  $\omega_{ref} = \omega_0$ . After being multiplied with the reference signal, the signal is low-pass filtered. As a result,  $\omega_0$  is removed from the signal, and Equation 2.8 can be written as Equation 2.9.

$$S(x, t) = |M_{xy}(x, t)| e^{-i(\Delta\omega(x)t + \phi_0)}. \quad (2.9)$$

## 2.4 The Gradient Recalled Echo Sequence

The previous section showed how a 1D image can be acquired using only a gradient in the x-direction. 2D and 3D imaging builds on the same principle, but is a bit more intricate, and requires a more complicated sequence. A sequence defines the timing of gradients, RF-pulses and the Analogue Digital Converter (ADC).

The Gradient Recalled Echo (GRE) sequence is one of the most common sequences in MRI. The sequence timing diagram is shown in Figure 2.6.

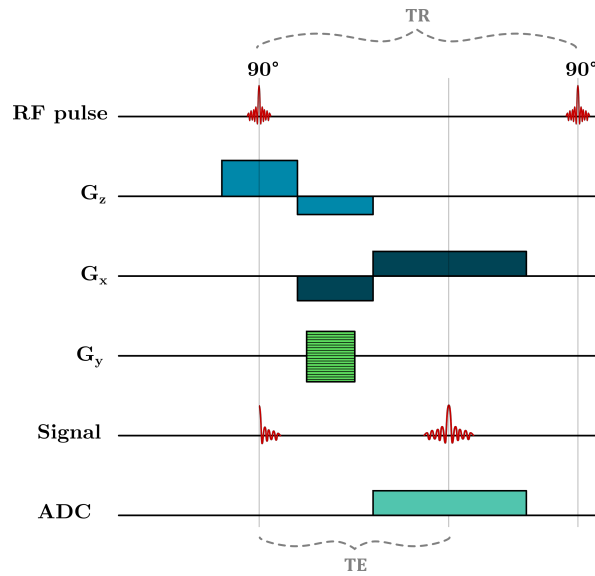


**Figure 2.6:** Gradient recalled echo sequence diagram. The diagram shows when the RF pulse is applied, when the three gradients are active, and when the ADC is switched on to record the produced signal.

Using the GRE sequence shown in Figure 2.6, 2D images of one or multiple slices can be acquired. Following is a brief introduction to how a 2D image is formed. For an in depth description of image formation, the reader is referred to the literature [5, p.141-176].

First, a slice of protons is excited. The excitation is done using an RF pulse along with a slice selective gradient, which in this case is the z-gradient  $G_z$ . See Figure 2.6. The protons are only excited if the RF-pulse frequency  $\omega_{rf}$  is approximately equal to the proton's precessional frequency  $\omega$ , which is given as  $\omega = \omega_0 + \gamma G_z z$  when the z-gradient is active. Thus implying that  $\omega_{rf}$  can be chosen to excite a slice of protons only at the desired z-position. This is illustrated in Figure 2.7.

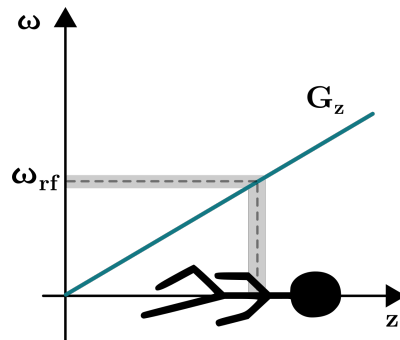


**Figure 2.7:** Slice selection. A slice is excited using an RF pulse along with an active z-gradient  $G_z$ . Due to the gradient, the protons along the z-axis will have different precessional frequencies  $\omega$ . Only the protons within the slice where  $\omega_{rf} \approx \omega$  will be excited.

After the slice has been excited, the protons within it are spatially encoded using the gradients  $G_x$  and  $G_y$ , as shown in Figure 2.6. In this example, the x-gradient is used for frequency encoding, while the y-gradient is used for phase encoding [5, p.153-164]. The frequency encoding is similar to the example in Section 2.3. Phase encoding is in essence the same as frequency encoding, but performed indirectly. The full details will not be provided here, but we will look at how the gradients manipulate and acquire data from the spins in k-space.

The key point in Section 2.3 was that the MR data is acquired in k-space, and that the inverse Fourier transform yields the final image. In order to get a 2D image, 2D k-space data must be acquired. The GRE sequence measures k-space line by line. Figure 2.8 shows how one line of k-space is acquired. One line of k-space is measured per Repetition Time (TR), which defined as the time interval between successive sequences applied to the same slice.

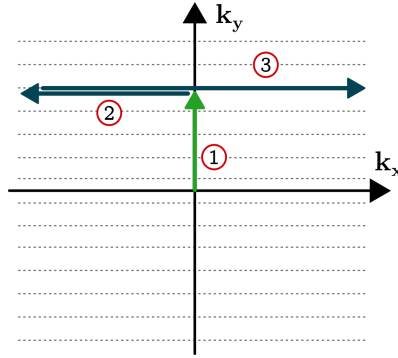


**Figure 2.8:** K-space scanning. After excitation, one line of k-space is acquired using the x and y gradients. (1) The protons are phase encoded using the y gradient. (2) The negative part of the x-gradient moves the spins in negative direction in k-space. (3) The positive gradient moves the spins through k-space in the positive direction again. As shown in Figure 2.6, this is when the ADC is switched on and the signal is recorded. A recalled echo is produced when the spins pass through the center of k-space.

The phase encoding gradient  $G_y$  determines which line of k-space is measured. The magnitude of the gradient is changed for each TR, meaning a new line of k-space is acquired. The lines in the y-gradient in Figure 2.6 represent the different gradient magnitudes, yielding different lines in k-space. In Figure 2.8, the y-gradient encodes the spins to a positive  $k_y$  value.

The x-gradient consists of two parts: one negative and one positive, where the positive has twice the duration as the negative. The effects of the gradient are illustrated in Figure 2.8. First, the spins are shifted towards negative  $k_x$  direction by the negative part of the gradient. The x-gradient's polarity is then switched to positive, and the spins will move towards the positive  $k_x$  direction in k-space. The ADC is turned on and samples the signal induced in the receive coils at the same time as the positive part of the x-gradient is active. As the spins pass through the center of k-space, a recalled echo is produced, as shown at the Echo Time (TE) in Figure 2.6. The sampled data from the ADC represents one line of k-space.

The sequence is repeated with different  $G_y$  values to acquire the entire k-space. Once the entire k-space is sampled, a 2D inverse Fourier transform converts the data to image space.

Similar to Equation 2.9, the signal produced at position  $r$  in the imaged slice after TE can be expressed as in Equation 2.10.

$$S(r) = |M_{xy}(r, TE)|e^{-i(\Delta\omega(r)TE + \phi_0)}. \quad (2.10)$$

Equation 2.10 shows that each pixel in the image holds a complex value. The magnitude value is determined by the transverse component of the net magnetization after TE. The phase is determined by the frequency offset due to inhomogeneity, and initial phase. This is shown in Equation 2.11.

$$\phi(r, TE) = \Delta\omega(r)TE + \phi_0. \quad (2.11)$$

Two images can be constructed from the complex pixel value: a magnitude image and a phase image. Figure 2.9 shows an example of both a magnitude and a phase image.

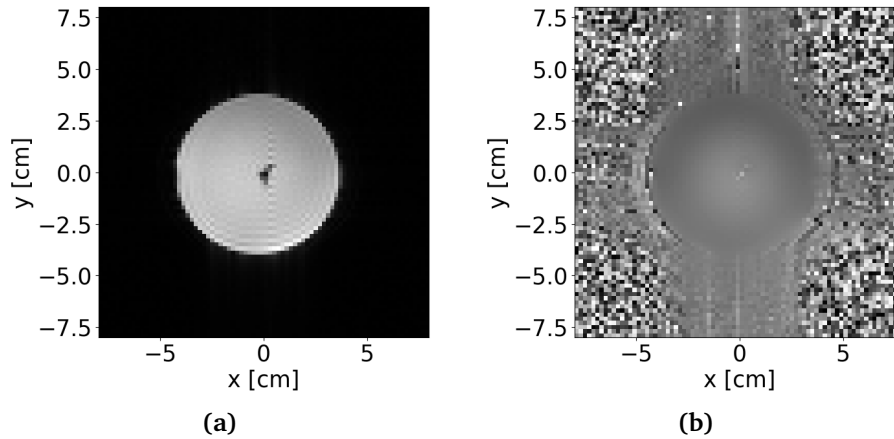


**Figure 2.9:** Magnitude and phase image. (a) Magnitude image of a circular phantom. Only where there are 1H protons, a signal is produced. The brighter the pixel value, the stronger is the signal. (b) Phase image of a phantom. Outside the phantom there is only noise with low signal strength and random phase. Some artifacts are visible outside the phantom.

## 2.5 Dual echo sequence

The values in the phase image acquired with a regular gradient recalled echo sequence are dependant on the initial phase, as shown in Equation 2.11. A dual echo sequence can be used to eliminate the initial phase from the equation, such that the phase values purely relate to the field inhomogeneity.

A dual gradient recalled echo sequence can be achieved in two different ways. Either two echoes at different echo times are produced within one TR, or the standard sequence from Figure 2.6 is run two times consecutively with two different echo times. An image is acquired at each echo time. In the first alternative the initial phase is the same for both images, while for the latter case it is assumed to be the same. By subtracting the two phase images, the resulting phase image is independent from the initial phase. This is shown in Equation 2.12, where  $\Delta TE$  is the difference between the echo times.

$$\phi(r, \Delta TE) = \Delta\omega(r)\Delta TE \quad (2.12)$$

The phase value in Equation 2.12 is the phase due to inhomogeneity acquired between the two different echo times.

## 2.6 SAR

Specific Absorption Rate (SAR) is a metric used to simulate and monitor heating in MRI. The SAR describes the rate at which RF energy is absorbed per unit mass [W/kg]. Being a measure of absorbed energy, it is used as an indirect measure of temperature increase. It is not possible to measure heating when performing a regular MRI scan, and SAR is therefore simulated before and during scanning to ensure heating is limited.

According to Maxwell's equations, the  $B_1$  field produced in the RF pulse is coupled with an electric field  $E$ . In a medium with electrical conductivity  $\sigma$ , the electric field sets up electric currents, which in turn results in heating of the medium. Heating is an unwanted effect of MRI, and thus needs to be controlled. As the electric field is non-measurable in MRI, it needs to be simulated to estimate the SAR. When imaging people, the simulations are run at digital human models.

The SAR at location  $r$  at time  $t$  during RF transmit can be found by Equation 2.13 [6].

$$SAR(\mathbf{r}, t) = \frac{\sigma(\mathbf{r})}{2\rho(\mathbf{r})} \cdot \|\mathbf{E}(\mathbf{r}, t)\|_2^2 \quad (2.13)$$

$\sigma$  is the electric conductivity,  $\rho$  the mass density and  $E$  the electric field. The SAR is usually averaged over a volume of interest, such as the entire body, the head or 10g of tissue/medium. The volume averaged SAR is calculated as in Equation 2.14, where  $V$  is the volume of interest.

$$SAR_{averaged}(\mathbf{r}, t) = \frac{1}{V} \int_V \frac{\sigma(\mathbf{r})}{2\rho(\mathbf{r})} \cdot \|\mathbf{E}(\mathbf{r}, t)\|_2^2 dV \quad (2.14)$$

In addition to averaging over a volume, SAR is averaged over time. SAR averaged over a specific volume and duration is used for defining safety limits. As large temperature increase can lead to tissue damage, regulatory limits of SAR are defined by the the International Electrotechnical Commission (IEC) and the U.S. Food and Drug Administration. For example, the average SAR values are restricted to 4W/kg for the body and 3.2W/kg for the head for a 6 min duration [7]. In addition, the temperature should never increase with more than 1°C. The 10g averaged SAR is simulated to monitor local hot spots. Figure 2.10 shows simulated 10g averaged SAR on a human body model.



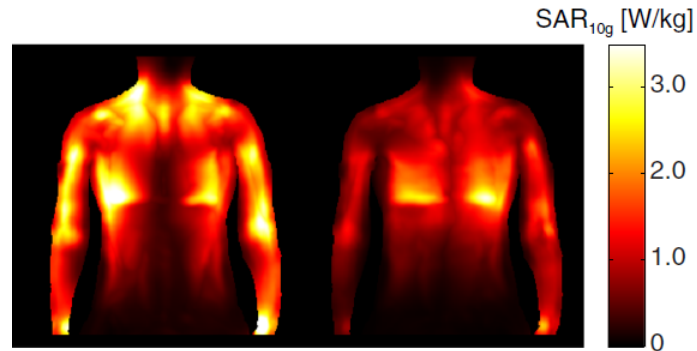


**Figure 2.10:** Simulation of 10g averaged SAR. Figure from Brink et al [8] under CC BY.

On an MR scanner, the SAR of a sequence is presented as a percentage. The percentage tells how much SAR the sequence is inputting compared to the maximum tolerated SAR before the safety limits are exceeded. The SAR percentage value is calculated and monitored continuously at the scanner to ensure the heating is safe.

As SAR is immeasurable and thus simulated, the quality of the simulations must be assured. By comparing the simulated SAR with the actual temperature increase in simple geometry phantoms, the quality of the simulation can be evaluated.

## 2.7 Ultra-High Field MR

Ultra High Field (UHF) MR is commonly defined as MR at a field strength of 7T or above, i.e.  $B_0 \geq 7T$ . Imaging at higher field strengths has both advantages and disadvantages. While scan times, resolution and Signal to Noise Ratio (SNR) can be improved, uniform excitation across the subject becomes more challenging. The imaged subject will also heat faster, meaning the SAR restrictions are more easily exceeded and therefore limiting.

Inhomogeneous excitation and faster heating are linked to a shorter wavelength of the RF pulses at higher field strengths. By looking at Equation 2.1, it is apparent that a higher field strength leads to a higher precessional frequency  $\omega_0$ . The RF pulse must match the precessional frequency. A higher frequency means a shorter wavelength and more energy, which results in more heating.

If the wavelength of the RF pulse is short enough to be at scale with the imaged object, standing waves can occur. At 7T, the wavelength is  $\approx 11\text{cm}$  in water. This means the excitation can become inhomogeneous. Inhomogeneity in the excitation field is referred to as  $B_1$  inhomogeneity. This results in an unwanted inhomogeneity in signal intensity as protons at different locations acquire different FAs.

A more serious effect of  $B_1$  inhomogeneity is local heating hot spots. Uneven excitation implies an uneven distribution of the energy. If not accounted for, the local hot spots cause a safety concern. The SAR safety limits must never be exceeded at any position, and monitoring 10g SAR is important to ensure the safety. This is of particular importance at UHF due to the shorter wave length.

Parallel Transmission (pTx) is used to mitigate the  $B_1$  inhomogeneities. pTx means that multiple transmit coils are driven independently of each other. The individual coil elements can then be combined and optimized to deliver an as homogeneous excitation as possible. pTx is a hot topic within UHF MR today.

## Chapter 3

# PRF Shift Thermometry

Building on the basics introduced in Chapter 2, this chapter shows how the chemical shift of water protons is utilized in PRF shift thermometry. It also discusses factors influencing the temperature measurements, such as magnet design, shimming and field drift. The chapter finish with a section discussing previous work within PRF shift thermometry. The sections 3.1-3.4 are based on previous work by the author [4].

### 3.1 Field Inhomogeneity and Phase

The magnetic field in an MR scanner will always be subject to inhomogeneities. The total field  $B_{tot}$  at position  $r$  can be expressed as

$$B_{tot}(r) = B_0 + \Delta B_0(r), \quad (3.1)$$

where  $B_0$  is the main static field, and  $\Delta B_0$  is the local inhomogeneity. As shown in Equation 2.11, the pixels' phase values in the final image depends on the field inhomogeneity through the term  $\Delta\omega(r)TE = \gamma\Delta B_0TE$ . This means that phase images can be used to image the field homogeneity. The phase value's dependence on inhomogeneity is utilized in PRF shift thermometry, where phase images are converted to images of temperature change.

There are several sources of inhomogeneity in MR. One such source is chemical shift, which is utilized in PRF shift thermometry. Chemical shift is explained in Section 3.2. While chemical shift is a wanted source of inhomogeneity in thermometry, other undesirable sources exists. The main magnetic field  $B_0$ , as shown in Figure 2.1, will never be perfectly uniform inside the scanner bore. Neither will the field from the gradients. In addition, any object will alter the magnetic field once placed in the scanner due to magnetic susceptibility. Shimming, as further described in Section 3.4, is used to improve field homogeneity.

### 3.2 Chemical Shift of Water Protons

Chemical shift is defined as a difference in the resonant frequency due to a difference in the molecular environment. For example, two  $^1\text{H}$  protons in two different molecules may have slightly different precessional frequencies due to different molecular environment. This is utilized in MR spectroscopy to find the presence and concentration of different metabolites within a volume of interest. While MR spectroscopy utilizes the different chemical shift of multiple molecules, PRF shift thermometry exploits the fact that the chemical shift of the water molecule changes with temperature [9]. To understand why, one must first understand the shielding effect.

Shielding is a diamagnetic susceptibility effect caused by the electrons. The electrons in a molecule surround the nuclei like a cloud. When placed in a strong magnetic field  $B_0$ , the electron cloud induces a small magnetic field opposing the main field. The induced field shields the nuclei from the external field, hence why it is called the shielding effect. Figure 3.1 illustrates how a proton is shielded by an electron cloud.

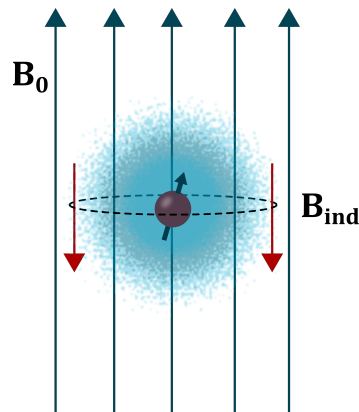


**Figure 3.1:** The shielding effect<sup>1</sup>. The electrons surrounding the nuclei sets up a field  $B_{ind}$  opposing the main static field  $B_0$ .

As a result of the shielding, the proton no longer experiences  $B_0$ , but a local field  $B_{loc}$  given by Equation 3.2.

$$B_{loc} = B_0 - B_{ind}. \quad (3.2)$$

Due to the shielding, the proton will precess with a frequency  $\omega_{loc} = \gamma B_{loc} \neq \gamma B_0$ . The amount of shielding depends on the temperature. With the water molecule as a basis, we will now look into how temperature affects the shielding of the  $^1\text{H}$  protons in the molecule. Water is the largest source of signal in MR, and also has

<sup>1</sup>Figure inspired from figure at: <https://mriquestions.com/chemical-shift.html>, Accessed: 09.12.21

a temperature dependence of the chemical shift that is independent of tissue type [9]. It is therefore used for PRF shift thermometry.

Water molecules bond to each other with hydrogen bonds. The bonds occur between the oxygen atom of one molecule, and one of the two hydrogen molecules from the other molecule. Figure 3.2 illustrates the bonding between water molecules.

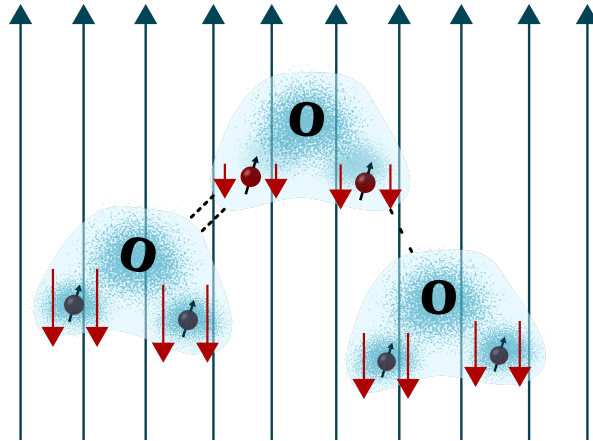


**Figure 3.2:** Hydrogen bonding of water molecules<sup>2</sup>. The  $^1H$  proton is less shielded when forming a hydrogen bond, or when the bond is bent/stretched. The leftmost molecule is hydrogen bonded to the middle molecule, resulting in less shielding for the the proton included in the bond. The bond between the middle and the rightmost molecule is being stretched/bent/broken. The protons not included in bonding are more shielded than those bonded.

When two water molecules form a hydrogen bond, the electron cloud surrounding the hydrogen proton is pulled away. As a result, the proton included in the bonding is less shielded, as illustrated in Figure 3.2. When the temperature increases, the hydrogen bonds will to a larger degree stretch, bend and break. Consequently, the molecules are spending on average less time in the bonded states. This means being on average more shielded, and as a result precess with a slightly lower frequency at higher temperatures. The relative change in PRF is related to the temperature change  $\Delta T$  as in Equation 3.3.

$$\frac{\Delta\omega_0}{\omega_0} = \alpha\Delta T \quad (3.3)$$

where  $\alpha$  is the temperature dependent coefficient of the water proton chemical shift given in ppm/ $^{\circ}C$ . For pure water  $\alpha$  has been experimentally shown to be about  $-0.01\text{ppm}/^{\circ}C$  [9].

<sup>2</sup>Figure inspired from figure at: <https://mriquestions.com/mr-thermography.html>, Accessed: 09.12.21

### 3.3 Measuring Temperature

So far it has been shown that the gradient recalled echo sequence can be used to acquire phase images, and that the phase values are linked to magnetic field inhomogeneity. It was further shown that the Proton Resonance Frequency (PRF) of water protons is temperature dependant due to chemical shift. This section aims to combine all that knowledge, and show how temperature change is estimated in PRF shift thermometry.

According to Equation 3.3, the PRF of water protons changes with temperature. This implies that the same proton will acquire different phase values when imaged at different temperatures  $T$ . This is exploited in PRF shift thermometry, where the first step is to acquire two phase images (as illustrated in Figure 2.9b) of the same slice.

The two phase images are taken with a dual gradient echo sequence. The first image is a reference image  $\phi^{ref}$ , taken at a reference temperature  $T_0$ . The change in phase  $\Delta\phi$  at position  $r$  in the image is found by subtracting the reference phase image from the second phase image  $\phi$ .

$$\Delta\phi(r) = \phi(r) - \phi^{ref}(r), \quad (3.4)$$

By inserting the phase expression from Equation 2.12, Equation 3.4 can be written as function of the field inhomogeneity.

$$\Delta\phi(r) = \gamma(\Delta B_0(r) - \Delta B_0^{ref}(r))\Delta TE. \quad (3.5)$$

The field inhomogeneity can be further split into two contributions [10]

$$\Delta B_0(T(r)) = \delta B_0(r) + Bc(T(r)). \quad (3.6)$$

The first expression  $\delta B_0$  is the inhomogeneity from the scanner components such as the magnet and coils, as well as the inhomogeneity resulting from the imaged object's own magnetic susceptibility. The latter expression  $Bc$  is the field inhomogeneity resulting from chemical shift, as discussed in Section 3.2. While the chemical shift depends on the temperature,  $\delta B_0$  is assumed to be temperature independent. Resulting, Equation 3.5 simplifies to the expression in Equation 3.7, where  $T_0$  is the temperature in the reference image.

$$\begin{aligned} \Delta\phi(T(r)) &= \gamma(Bc(T(r)) - Bc^{ref}(T_0(r)))\Delta TE \\ &= \gamma\Delta Bc\Delta TE \\ &= \Delta\omega_0\Delta TE. \end{aligned} \quad (3.7)$$

Equation 3.7 shows that the change in phase  $\Delta\phi$  is due to a change in precessional frequency  $\Delta\omega_0$  resulting from the chemical shift.

As described in Section 3.1, the relative change in precessional frequency due to chemical shift is proportional to the change in temperature  $\Delta T$ , as shown in

Equation 3.3. By combining Equation 3.3 and 3.7, the temperature change can be expressed as in Equation 3.8.

$$\begin{aligned}\Delta T(r) &= \frac{\phi(r) - \phi^{ref}(r)}{\alpha\omega_0\Delta TE} \\ &= \frac{\Delta\phi(r)}{\alpha\gamma B_0\Delta TE}\end{aligned}\quad (3.8)$$

$B_0$ ,  $\alpha$ ,  $\gamma$  and  $\Delta TE$  are known values, meaning the measured phase can be transformed to a temperature change estimate by Equation 3.8.  $\Delta\phi$  is found by taking two phase images. The first is a reference image at temperature  $T_0$ , while the second is a phase image taken at temperature  $T$ . The reference image is then subtracted from the second image. This phase change image is then transformed into a temperature change image by Equation 3.8. An example of a temperature change image is shown in Figure 3.3. Each pixels holds a temperature change value, and the image describes the temperature change in the object.

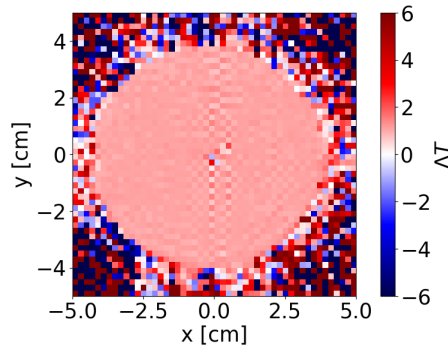


**Figure 3.3:** Temperature map of a phantom. Outside of the phantom is only air, thus the temperatures measured there is only noise. The map shows the temperature change relative to the temperature in a reference image.

The temperature change value in each pixel tells how the temperature has changed in the second image compared to the reference image.

Instead of taking only two images, a series of images can be acquired. Using the first image as a reference image, the rest of the images can be transformed into temperature change images. This way the series of images depicts how the temperature changes over time relative to the first reference image.

### 3.4 Magnet Design and Shimming

PRF shift thermometry, as described in Section 3.3, builds on the assumption that chemical shift is the only magnetic field inhomogeneity that changes with time and temperature. This is not true in real life. The scanner field changes slightly during scanning in what is called magnetic field drift, which is further explained

in Section 3.5. To understand why the field drift occurs, it is important to understand how the scanner is built. This section aims to show the main components of a scanner, how the field inhomogeneity is improved by shimming, and discuss possible sources of magnetic field drift.

The three main components of an MR scanner are the main magnet/coil, gradient coils and RF coils. An example of the physical setup of all the components is shown in Figure 3.4.

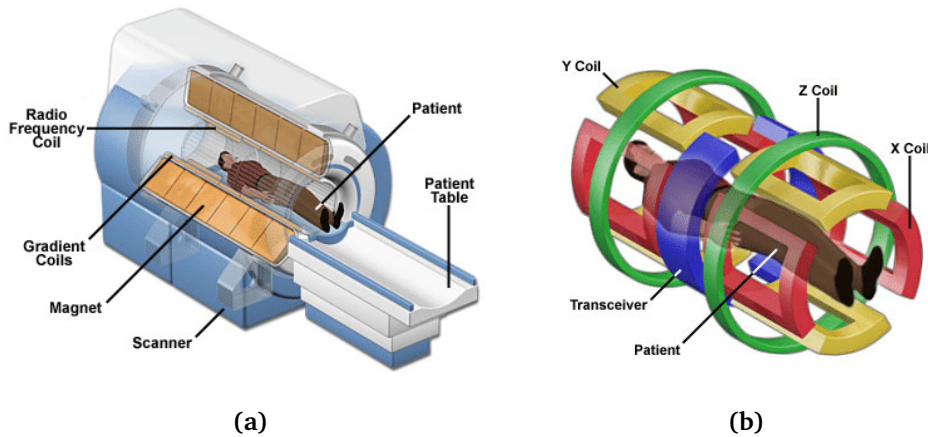


**Figure 3.4:** Magnet design and coils<sup>3</sup>. (a) Scanner components. (b) Gradient coils. The transceiver coil is an RF coil used for both transmit and receive.

The main magnet/coil is typically cooled with liquid helium, whereas the gradient coils are cooled by water.

The above components are the main elements needed to acquire an image. The  $B_0$  field in such a setup is however not very homogeneous, and will be further altered by the imaged objects own magnetic susceptibility.

Therefore, shimming is performed to make the field more homogeneous. Shimming is the process of improving the  $B_0$  homogeneity by adding magnetic fields. This is illustrated in Figure 3.5.

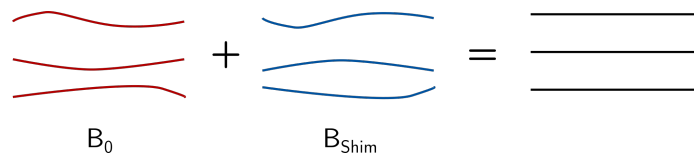


**Figure 3.5:** Concept of shimming. Magnetic fields improving the  $B_0$  homogeneity are added by passive and active shimming.

Shimming is performed passively and actively. Passive shimming improves the  $B_0$  homogeneity by placing ferromagnetic material into slots in the scanner. The

<sup>3</sup>Figures from: Caligari Conti, Daphne. (2016). Magnetic Resonance Imaging.



ferromagnetic material alters the field, and by careful placement the field homogeneity can be improved. The passive shimming is performed by a technician when installing the scanner.

Active shimming is shimming performed by coils by both dedicated shim coils as well as the gradient coils. By passing a constant current through the coils, they set up a field which can be used to improve the homogeneity. Shimming coils are illustrated in Figure 3.6.

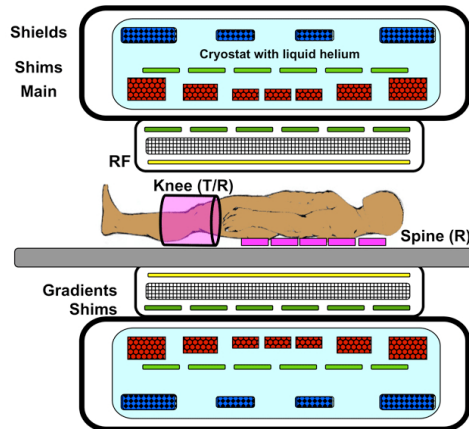


**Figure 3.6:** Shimming coils are used for making the magnetic field more homogeneous<sup>4</sup>.

The shimming coils are cooled either by liquid helium or water, depending on the scanner.

Active shimming is performed by taking an image of the field homogeneity by acquiring a  $B_0$  map. This can be done with a GRE sequence as described in Section 2.4. After a  $B_0$  map is taken, the current through the shim coils are optimized to improve the field homogeneity. Then, a new  $B_0$  map is acquired and optimized, and the field homogeneity is iteratively improved.

When the scanner is set up for the first time, the shim currents are optimized for a standard spherical phantom. The shim current values are then saved and can be used for shimming. This is called a Tuneup shim.

Instead of using the shimming optimized for a specific phantom, a shimming optimizing procedure can be performed on the imaged subject. This is referred to as a Standard shim. The iterative procedure described above is then performed for the imaged object, which could be another phantom, a person or any other object.

<sup>4</sup>Figure from: <https://mriquestions.com/many-kinds-of-coils.html>, Accessed: 13.12.21

### 3.5 Magnetic Field Drift

Magnetic field drift is defined as change in the main magnetic field  $B_0$  over time. It has been demonstrated by Bing et al. that field drift is linked to the bore temperature[2]. By comparing two sequences of different duty cycles, it was found that the sequence with the highest duty cycle resulted in the largest temperature increase and field drift.

One source of field drift could be heating of the gradient coils. Large electric currents are passed through coils to generate the magnetic fields, which. As a result they are heated. As the gradient coils are cooled by water, they are extra prone to heating. The same is true for water cooled shim coils. As the coils are heated, the geometry of the coil can be altered as the metal expands. The resistivity of metal also increases with temperature. Altogether, this can lead to field drift. Other possible sources are gradient heating of passive shims and temperature dependant changes in magnetic susceptibility[2].

The magnetic field drift results in change in the phase images, and therefore introduces errors in the temperature maps. In a study performed by Bing et al., uncorrected field drift in a phantom resulted in a temperature error of  $77^\circ\text{C}$  after 60 minutes [2]. A 3T scanner was used for the experiment.

The drift can be decomposed into contributions of different orders. Figure 3.7 illustrates 0th, 1st and 2nd order spatial magnetic field drift in a temperature map.

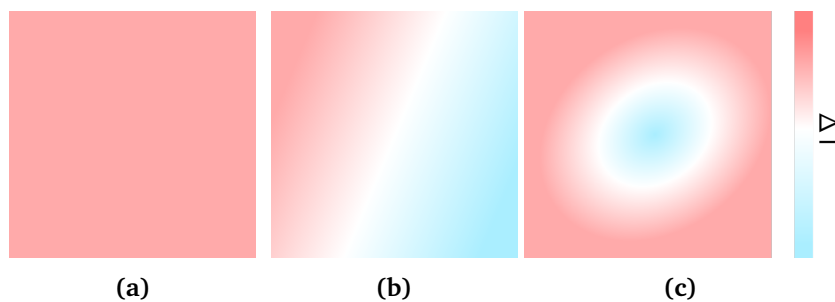


**Figure 3.7:** Illustration of the three first orders of decomposed spatial field drift. Each image illustrates a temperature map taken of unheated material. Without field drift, all images should be completely white, i.e.  $\Delta T = 0$ . (a) 0th order. (b) 1st order. (c) 2nd order.

Not that the orders of drift referred to are the drift order in space, not in time. 0th order spatial drift is an equal amount of drift across the entire image, which increases in magnitude with time. 0th order drift is illustrated in Figure 3.7a. 1st order spatial drift is a linear gradient with a given angle, and a slope that increases with time. This is shown in Figure 3.7b. Finally, 2nd order spatial drift is radial and with increasing magnitude with time, see Figure 3.7c.

### 3.6 Related work

Using the change in PRF due to chemical shift for thermometry was first introduced by Ishiara et al. in 1995 [9]. The method was tested both at a phantom and in vivo. A continuous wave was used for inductive heating, and the cooling was measured using PRF shift thermometry. In the pure water phantom experiment, the temperature in the centre of the phantom increased with 10°C. After heating, the phase was measured using a GRE sequence. The phase images were then converted into temperature maps, as shown in Equation 3.8. A ROI was used to remove the thermal inhomogeneities due to the inductive heating, as well as removing the dispersion in the phase images due to noise. An accuracy of more than  $\pm 0.5^\circ\text{C}$  within a few seconds/slice was obtained for the pure water phantom. The experiments were performed at a 4.7T scanner. The coefficient  $\alpha$  describing the temperature dependence of the chemical shift was also estimated. It was shown that the coefficient was almost the same for different materials with chemical composition similar to living tissues.

After being introduced by Ishiara et al., PRF shift thermometry has made its way into practical applications. A challenge with the method is its sensibility to magnetic field drift, and for most practical cases the drift must be corrected for to obtain an acceptable accuracy. A study performed by Bing et al. found that PRF shift thermometry with a combined drift correction algorithm delivered a sufficient accuracy for guiding mild hypothermia treatments with MR-HIFU (High-Intensity Focused Ultrasound) [2]. Experiments were carried out at a tissue mimicking phantom and in a rabbit. Using center-frequency adjustment along with a combined drift correction algorithm, they achieved an accuracy of  $0.57 \pm 0.58^\circ\text{C}$  in the heated region, and  $0.54 \pm 0.42^\circ$  in the unheated region. A central part of their drift correction algorithm was to use the unheated areas to remove the magnetic field drift from the estimates. A 3T scanner was used in the study.

As MR imaging itself causes heating, measuring the RF induced heating is of interest. Both to validate SAR calculations, and to ensure the safety of metallic implants. In a study performed by Ehses et al., PRF shift thermometry was used to map the RF induced heating along conductive wires [3]. The method can be used in implant safety investigations. By adding a heating pulse to a gradient recalled echo sequence, images could be acquired while effectively heating the wire. This way RF induced heating could be measured while scanning, providing a better option than using fluoroptic temperature probe, as a probe can only measure one point and is prone to displacement errors. The wire was imaged with the heating sequence for 7 minutes at a 1.5T scanner. The end of the wire heated approx.  $7^\circ\text{C}$  during the session. The temperature change within a ROI was compared to temperature measurements from a fluoroptic probe, and resulted in somewhat similar heating curves.

In a study by Wang [11], the RF shift thermometry method was evaluated at a 7T system. By using an agarose gel phantom, the temperature coefficient was estimated, before the accuracy of the method was evaluated ex vivo in beef

muscle, and in vivo in a rat using focused ultrasound heating. The study confirmed the sensitivity  $< 1^{\circ}\text{C}$  of PRF shift thermometry at 7T.

PRF shift due to chemical shift is one of multiple ways to do thermometry in MR. For description and comparison of PRF shift thermometry and other thermometry methods, the reader is referred to Rieke and Pauly [10] and Lutz and Bernard [12].

## Chapter 4

# Method

This chapter shows how PRF shift thermometry, as described in Chapter 3, was implemented and evaluated on an RF-heated phantom. First, the overall setup of all the physical components is shown in Sections 4.1. Section 4.2 contains the details on the custom phantom that was built for the experiments in this report. A custom acquisition sequence was also made, which is presented in Section 4.3. The sequence acquisition parameters that were used for the experiments are described in Section 4.4. Section 4.5 and 4.6 details the temperature map formation pipeline and drift correction. The experiments performed to evaluate the PRF shift thermometry method are described in Section 4.8. Finally, Section 4.9 shows how the final series of temperature maps were evaluated.

### 4.1 Setup

The MR scanner used in the experiments in this report was a 7T Siemens MAGNETOM Terra<sup>1</sup>. The coil used for RF transmit and receive was a Nova 1Tx/32Rx head coil. Figure 4.1 shows the scanner and the head coil.

---

<sup>1</sup>Siemens Healthineers. (2022). *MAGNETOM Terra: Translate 7T research power into clinical care* [Brochure]. <https://www.siemens-healthineers.com/magnetic-resonance-imaging/7t-mri-scanner/magnetom-terra>



**Figure 4.1:** (1) Siemens MAGNETOM Terra MR scanner. (2) Nova 1Tx/32Rx head coil.

A custom agar phantom was made for the experiments, see Section 4.2 for full details on the phantom. Figure 4.5 shows an image of the phantom. The temperature in and around the phantom was monitored with a fiber optical temperature sensor system from OSENSA<sup>2</sup>, specifically designed for use in MRI. The fiber optic probes (PRB-100-02M-STM-MRI) has an accuracy of  $\pm 0.1^{\circ}\text{C}$  with a response time of 1.5s. The temperature data was logged on a computer connected to the transmitter (FTX-300-LUX+) by a USB cable. The computer and transmitter were placed in the MR control room. The temperature probes were connected to the transmitter by extension cables (EXT-100-10M-STM-STM) going through the wall from the control room to the scanner room. Non-magnetic fiber couples (ACC-CON-STM-STM) were used to connect the probes to the extension cables. The probes were then placed in and around the phantom. Figure 4.2 shows the agar phantom with temperature probes placed in the coil.

---

<sup>2</sup>OSENSA. (2019). *MRI and Research Fiber Optic Temperature Sensors* [Data Sheet]. [https://www.osensa.com/uploads/content/DATASHEET-DMK-0010A-5,%20MRI%20RESEARCH%20APPLICATIONS%20\(1\).pdf](https://www.osensa.com/uploads/content/DATASHEET-DMK-0010A-5,%20MRI%20RESEARCH%20APPLICATIONS%20(1).pdf)

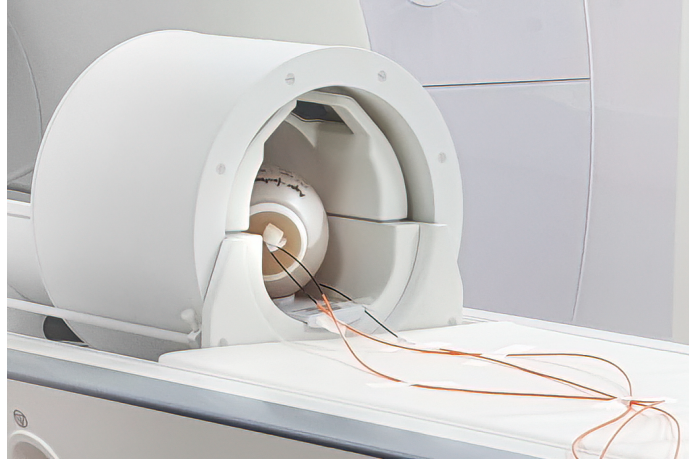


**Figure 4.2:** Phantom and temperature probes placed in the coil. Two temperature probes (A and B) were placed inside the agar gel, while one probe (C) measured the temperature of the air just outside of the phantom.

The non-spherical geometry of the agar gel at the opening of the phantom affects the images negatively. The agar phantom was therefore placed at an angle in the coil, so that the opening would not be in the central sagittal and transversal planes. This is illustrated in Figure 4.3.

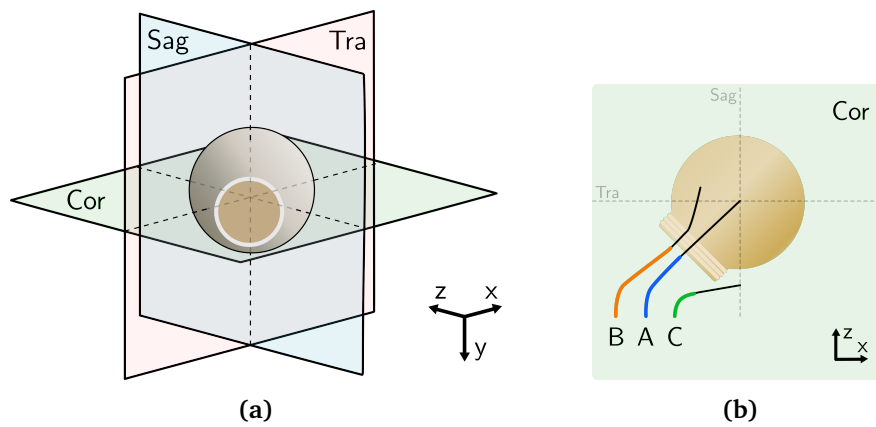


**Figure 4.3:** Orientation and placement of the phantom and temperature probes. (a) The phantom orientation relative to the sagittal, coronal and transverse plane. (b) Ideal placement of the temperature probes. Probe A should be placed in the center of the phantom and probe B towards the edge. Both should lay in the central coronal plane.

The ideal probe placement is shown in Figure 4.3b. The aim was to place probe A in the center of the phantom, probe B between the center and the edge and C outside of the phantom to measure the air temperature. The probes were inserted into the phantom by hand. Localizer images of the phantom with the OSENSA temperature probes inserted are shown in Figure 4.4.

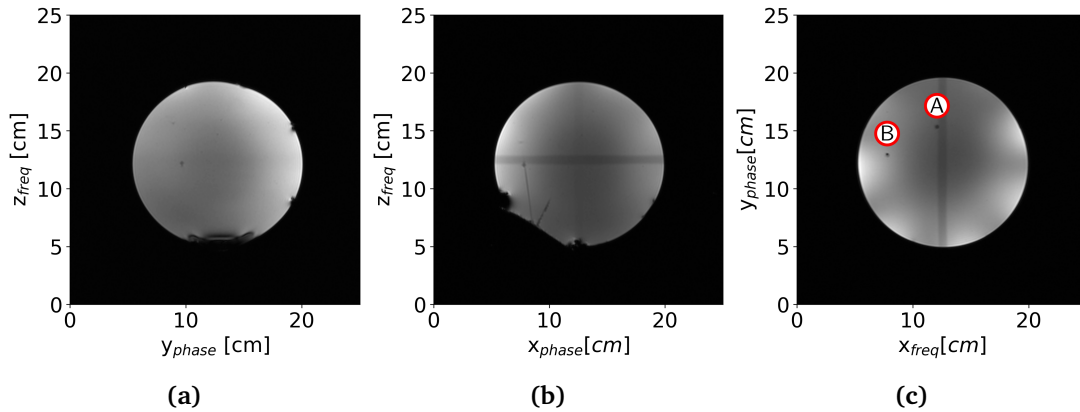


**Figure 4.4:** Localizer images of the agar phantom in all three planes. (a) Sagittal view. (b) Coronal view. The black lines coming in from the bottom left of the phantom are the temperature probes A and B, see Figure 4.3b. (c) Transversal view. The two black points are the temperature probes A and B.

Figure 4.4b and 4.4c shows the actual probe placements. Probe B was placed reasonably well in the central coronal plane, while probe A was  $\approx 3\text{cm}$  off-center.

## 4.2 Custom Phantom

A custom spherical agar phantom was made for the experiments. The phantom had a diameter of 150mm, and a conductivity of  $\approx 1.13\text{S/m}$ . The phantom is shown in Figure 4.5.



**Figure 4.5:** Agar phantom.

The purpose of the custom phantom was to have a spherical object to measure the RF-induced heating. The phantom was made with agar gel so that temperature probes could be inserted without the risk of spilling (in contrast to a liquid phantom). In addition, it was desired that the conductivity of the phantom was approximately  $1\text{S/m}$ , and without any fat or other substances. The phantom was basically salt water in gel form.



A spherical lamp cover of plastic was used as a container for the agar gel<sup>3</sup>. The agar gel was made using the ingredients in Table 4.1.

**Table 4.1:** Phantom ingredients.

Ingredient	Amount [g]
Milli-Q Water	2000
Difco Bacto-Agar	53.83
Sodium Azide (NaN <sub>3</sub> )	2.41
Sodium Chloride (NaCl)	10.04

According to a study performed by Bennet on agar gel conductivity, the conductivity using the ingredients in Table 4.1 should be  $1.13 \pm 0.1 \text{ S/m}$  [13]. The agar phantom was made as follows:

1. First, the Milli-Q water was measured and put on boil on a plate with a magnetic stirrer, see Figure 4.6a.
2. 10.04g of salt was added when the water was  $\approx 42^\circ\text{C}$
3. Sodium azide was added when the mixture was  $\approx 70^\circ\text{C}$ .
4. The powder agar was added when the mixture was  $75 - 80^\circ\text{C}$ .
5. The mixture was then set to boil for 30 minutes at  $75 - 80^\circ\text{C}$ , see Figure 4.6b.
6. After boiling, the mixture was cooled to about  $45 - 50^\circ\text{C}$ .
7. The mixture was then poured into the plastic container, where it was left for approximately 24 hours to solidify. See Figure 4.6c.
8. After 24 hours, the phantom was sealed with silicon lids and tape. This was done so that the agar gel would not dry out.

Figure 4.6 shows step 1, 5 and 7 of the above process.

---

<sup>3</sup>Clas Ohlson. (2022). *Lampekuppel* [Webpage]. <https://www.clasohlson.com/no/Lampekuppel/p/32-4391>

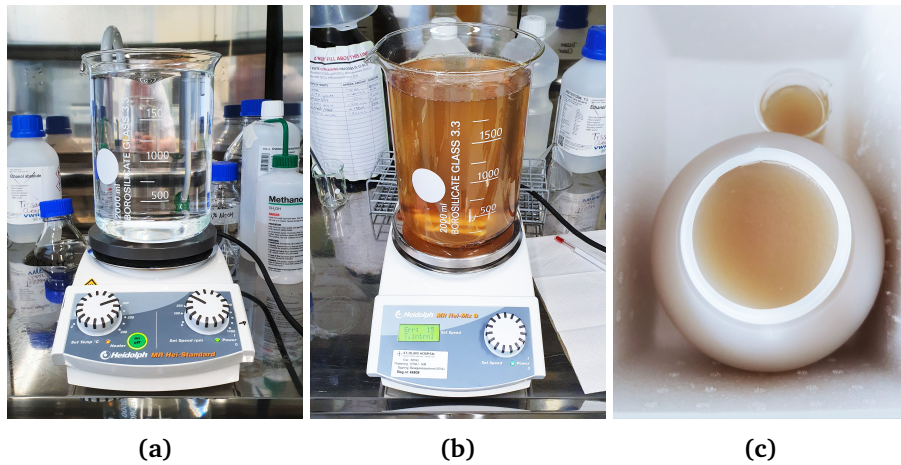


**Figure 4.6:** Phantom cooking process. (a) Water was put to boil on a cooking plate with built in magnetic stirrer. (b) The mixture with all ingredients added. (c) The solidified mixture in the plastic container after 24 hours of resting.

After the phantom was finished, it was placed in a cabinet in the MR scanner room where it was stored between all experiments.

### 4.3 Custom GRE Sequence With Adjustable SAR

For the experiments, it was desirable to evaluate the temperature maps from sequences with different SAR. To be able to adjust the SAR value of the sequences without altering the sequence parameters, a custom gradient recalled echo pulse sequence with an added heating pulse was implemented. The heating sequence was inspired by Ehses et al.[3]. A Gradient Recalled Echo (GRE) sequence from Siemens was used as a base for the custom sequence. The sequence was a dual echo sequence as described in 2.5.

The fat saturation option of the sequence was turned into a controllable heating pulse. Fat saturation consists of an RF pulse and spoiler gradients, which are added to the start of the sequence. The RF pulse is set to the resonance frequency of protons in fat, so that only these protons are excited. The protons are then dephased by the spoiler gradients to kill the signal.

As the custom phantom from Section 4.2 did not contain fat, the RF pulse of the fat saturation was off-resonance and purely contributed to heating. Control of the heating was added by enabling the user to change the flip angle of the RF pulse. At the scanner, the flip angle was determined by the RF pulse amplitude, and not duration. Increasing the flip angle thus meant an increase in the RF pulse amplitude, resulting in more inputted energy and a higher sequence SAR. This way the SAR could be increased as desired. The FA could be set to 0 and up to system maximum. The spoiler gradients were not removed, and were thus a part of the custom sequence. Figure 4.7 shows the customized fat saturation at the start of the GRE sequence.

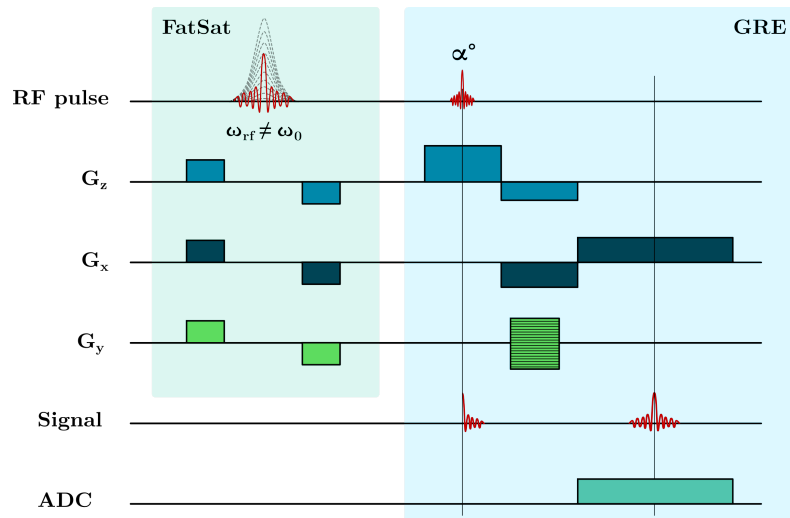


**Figure 4.7:** Custom GRE sequence with tunable SAR. Fat saturation was added at the start of the gradient recalled echo sequence to increase the SAR. The fat saturation RF pulse was off-resonance (no fat in the phantom) and therefore contributed to heating only. The user could indirectly control the amplitude of the RF pulse by adjusting the flip angle, which in turn gave control of the amount of heating. This way the SAR of the sequence could be increased as desired. The spoiler gradients at  $G_z$ ,  $G_x$  and  $G_y$  were a part of fat saturation.

The sequence was developed using Siemens' sequence programming tool IDEA. Due to confidentiality reasons the code can not be shared.

#### 4.4 Sequence Setup Parameters

The sequence from Section 4.3 was run with two different sets of parameters, which will be referred to as the Standard sequence and the Whisper sequence. The parameters for both setups are shown in Table 4.2.

**Table 4.2:** Standard sequence parameters.

Sequence Name	Standard	Whisper
Sequence Type	Spoiled Gradient Recalled Echo	Spoiled Gradient Recalled Echo
TR	60ms	60ms
TE	3.06ms, 4.08ms	4.82, 5.84
Number of Echos	2	2
Flip Angle	24°	15°
Number of Slices	3	3
Slice Orientation	Transversal	Transversal
Repetitions	77	77
Slice Thickness	4mm	4mm
Spacing Between Slices	28mm	36mm
Rows, Columns	64, 64	64, 64
Pixel Spacing	[4mm, 4mm]	[4mm, 4mm]
FOV	[256mm, 256mm]	[256mm, 256mm]
Number of Averages	1	1
Gradient Mode	Fast	Whisper
FatSat Flip Angle	0-360°	0-360°

The SAR of both the Standard and Whisper sequence was controlled through the fat saturation flip angle.

The Whisper sequence setup was designed to have the same Repetition Time (TR) as the Standard sequence, but using whisper gradient mode. In whisper gradient mode the gradient rise times are increased, which reduces the sound produced by the gradients. The Whisper sequence was used to evaluate correlation between magnetic field drift and gradient usage.

Using either of the tow sequence setups, 77 images were taken of each of the three slices, i.e. a total of 231 images. This will be referred to as one image series, and is illustrated in Figure 4.8.

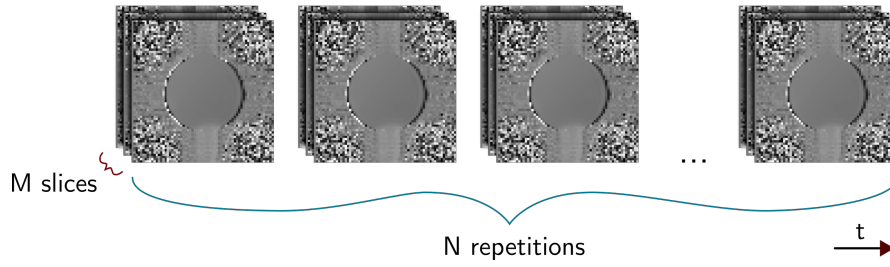


**Figure 4.8:** A series of images. One series consists of  $N=77$  images taken of  $M=3$  slices.

Acquiring one image series took 10 minutes.

The different slices will be referred to slice 1, 2 and 3. The  $z$  position of the slices for both sequences are shown in Table 4.3.

**Table 4.3:** Slice  $z$ -positions relative to the isocenter.

	Slice 1	Slice 2	Slice 3
Standard	-28mm	0mm	28mm
Whisper	-36mm	0mm	36mm

## 4.5 Temperature Map Formation Pipeline

After the phase images were acquired, they were converted to temperature maps. The temperature maps were calculated separately for each slice. All the phase images of the same slice were extracted from the image series in Figure 4.8, leaving a sequence of images as shown in Figure 4.9.

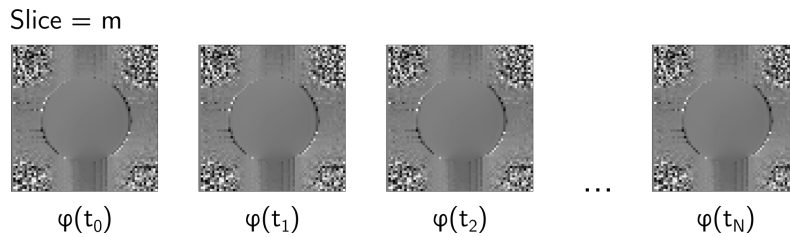


**Figure 4.9:** Sequence of phase images from one slice. There are in  $N$  images of slice  $m$  in one image series.

The first phase image of the slice was used as a reference image. Each subsequent image was then converted to a temperature map as shown in Figure 4.10.

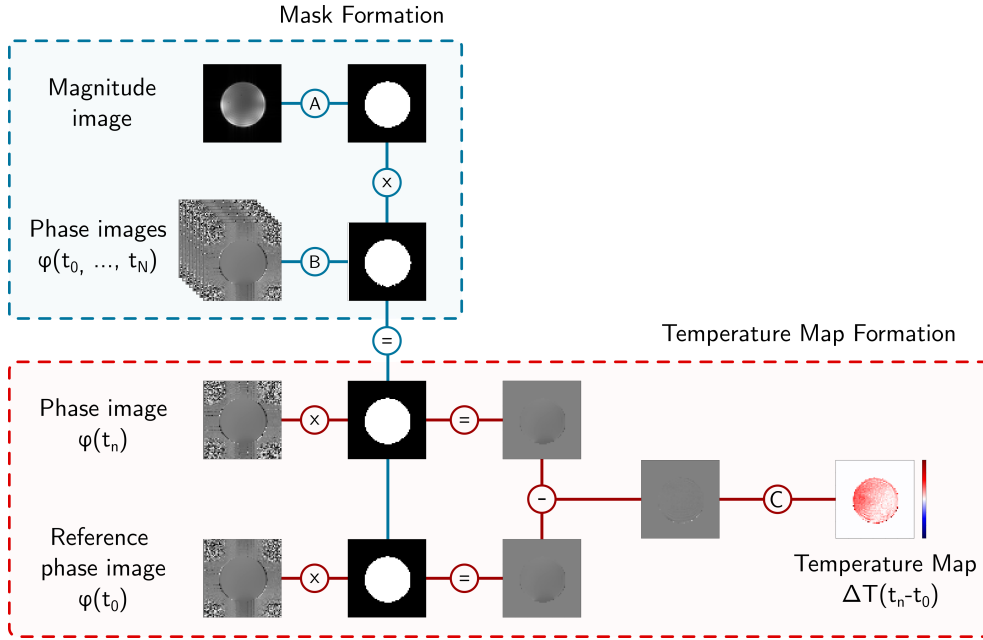


**Figure 4.10:** Temperature map formation. The temperature map shows the temperature change between a phase image from time  $t_n$  and a reference phase image at time  $t_0$ . First, the two phase images were masked. A combined mask was generated by (A) masking away pixels with low signal intensity in the magnitude image, and (B) masking the noisy pixels with a high standard deviation across all phase images in a series. The masked phase images were then subtracted and (C) converted, by using Equation 3.8, to temperature maps showing the estimated temperature change  $t = t_n - t_0$  after the reference phase image.

Before being converted to temperature maps, the phase images were masked. The mask was made by combining a magnitude mask with a standard deviation mask.

The magnitude mask filtered the pixels with a low signal intensity, as those pixels contained the air around the phantom. The mask was generated by applying the operation in Equation 4.1 on a magnitude image of the slice. Pixels with a signal intensity lower than a threshold value were masked. This is denoted as operation A in Figure 4.10.

$$MagMask_{i,j} = Bool(S_{i,j} > T_{Mag}) \quad (4.1)$$

In Equation 4.1  $i$  and  $j$  are pixel indices,  $S$  is the magnitude image pixel value and  $T_{mag}$  is the threshold value. The threshold was chosen manually by the author for each series of images.

The standard deviation mask removed the noisy pixels with a high standard deviation across all the images in the series. Denoted as operation B in Figure 4.10, the mask was generated by applying Equation 4.2 at the phase images of the slice.

$$StdMask_{i,j} = Bool(\sigma_{i,j}(\phi_{i,j}(t_0, \dots, t_N)) < T_{Std}) \quad (4.2)$$

$\sigma_{i,j}$  is the standard deviation of the pixel's values across all the phase images of the slice, while  $T_{Std}$  is the threshold value.  $T_{Std}$  was as  $T_{Mag}$  chosen manually to a reasonable value by the author. Both masks were combined to one mask, which was used to mask the phase images.

After both images were masked, the reference phase image was subtracted from the other phase image. Instead of simply subtracting the phase values, they were subtracted by using complex exponentials as shown in Equation 4.3. This was done to avoid possible phase wrappings[14].

$$\begin{aligned}\Delta\phi_{i,j} &= \phi(t_n) - \phi(t_0) \\ &= \angle(e^{i\phi_{i,j}(t_n)}(e^{i\phi_{i,j}(t_0)})^*)\end{aligned}\quad (4.3)$$

The  $\Delta\phi$  image was then converted into a temperature map by applying Equation 3.8 at each pixel. This is denoted as operation C in Figure 4.10, and written out in Equation 4.4.

$$\Delta T_{i,j} = \frac{\Delta\phi_{i,j}}{\alpha\gamma B_0\Delta TE}\quad (4.4)$$

The following values were used:  $\alpha = -0.01\text{ppm}$ ,  $\gamma = 2.675 \cdot 10^8\text{rad/s/T}$ ,  $B_0 = 7\text{T}$  and  $\Delta TE = 1.02\text{ms}$ .

The temperature map formation shown in Figure 4.10 was done for all the phase images of slice  $m$  in a series. Resulting was a sequence of images showing the temperature evolution in that slice. This is illustrated in Figure 4.11. Note that as the first image was used as a reference image, the sequence of temperature images contain  $N - 1$  images, as opposed to the  $N$  phase images shown in Figure 4.9.

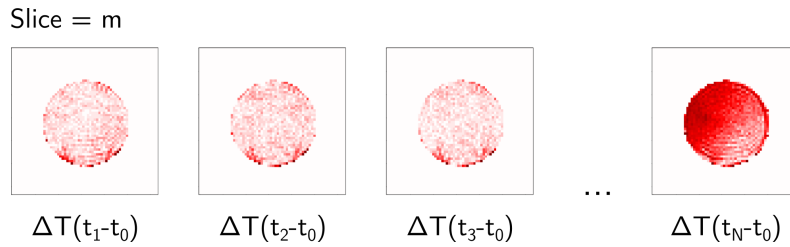


**Figure 4.11:** Sequence of temperature images from one slice. The first phase image is used as a reference, meaning there are  $N - 1$  temperature maps in the sequence of temperature images from slice  $m$ .

The implementation of the temperature map formation can be seen in Listing C.1 in Appendix C.1.

## 4.6 0th Order Spatial Drift Correction

This section shows how 0th order spatial field drift was removed from the raw temperature maps. The process consisted of two steps:

1. Estimate the spatial 0th order drift.
2. Subtract the spatial 0th order drift from the raw images

Both steps are described in detail below. The implementation of 0th order drift correction in Python can be viewed in Listing C.2 in Appendix C.2.

### Estimating the spatial 0th order drift

First, the 0th order spatial drift was estimated. This was done individually for each slice. I.e. a sequence of 76 (N-1) temperature maps, as shown in Figure 4.11, was used. As 0th order drift is equal across the image, temperature probe A was used to subtract the drift. The drift during the sequence of images was estimated by comparing the temperature data from probe A with the mean temperature from a 9 pixel Region of Interest (ROI) centered around the placement of the temperature probe in the image. The ROI is marked as a white square in Figure 4.12b.

The mean  $\Delta T(t_n - t_0)$  value within the ROI was calculated for all N-1 temperature maps. The temperature from probe A was then subtracted to find the error of the ROI estimate. This error was assumed to be the 0th order drift with noise. The 0th order drift  $D_0(t_n - t_0)$  was then estimated by performing linear regression on the error data. This is illustrated in Figure 4.12a.

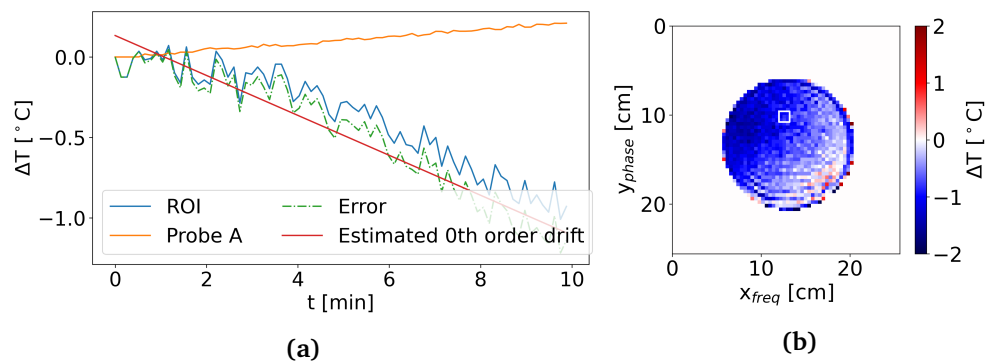


**Figure 4.12:** 0th order drift estimation. (a) Illustration of 0th order drift estimation. The temperature measured with probe A was subtracted from the ROI estimates to find the error of the estimates. The 0th order drift was estimated by linear regression on the error data. (b) Temperature map showing the 9 pixel ROI used to acquire the ROI  $\Delta T$ . The ROI is marked by the white square.

The temperature data from probe A had to be interpolated to fit the ROI data from the images. This was performed by using the function `numpy.interp` from



NumPy<sup>4</sup>. The linear prediction was then done using `sklearn.linear_model.LinearRegression` from scikit-learn<sup>5</sup>.

### Subtracting the spatial 0th order drift from the images

After estimating the spatial 0th order magnetic field drift, the estimate  $D_0$  was subtracted from the temperature maps  $\Delta T$ . This was done by subtracting the estimated drift value  $D_0(t_n - t_0)$  from all pixels within the mask of the temperature map  $\Delta T(t_n - t_0)$ . Doing this for all temperature maps yielded a sequence of 0th order drift corrected images  $\Delta T_0$ . The subtraction of 0th order drift is demonstrated in Figure 4.13.

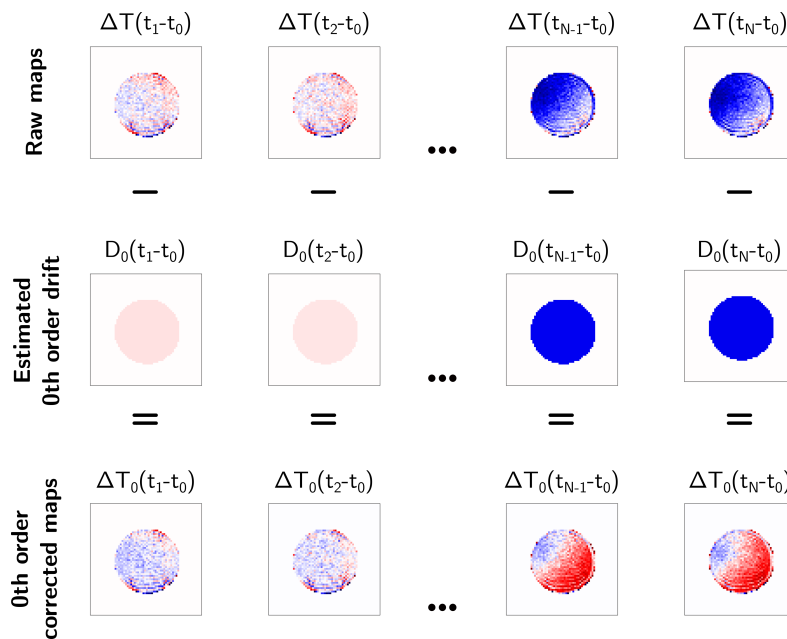


**Figure 4.13:** Subtraction of 0th order drift. The estimated 0th order drift  $D_0(t_n - t_0)$  was subtracted from the raw temperature map  $\Delta T(t_n - t_0)$ . This was done for all images, yielding a sequence of temperature maps corrected for 0th order drift, denoted as  $\Delta T_0$ .

## 4.7 1st Order Spatial Drift Correction

1st order spatial drift correction was applied to the 0th order corrected images, shown as the bottom row in Figure 4.13. As shown in Section 3.5, 1st order spatial field drift is a linear gradient across the image. The gradient was assumed to have

<sup>4</sup>NumPy. (2022). *numpy.interp* [Webpage]. <https://numpy.org/doc/stable/reference/generated/numpy.interp.html>

<sup>5</sup>scikit-learn. (2022). *sklearn.linear\_model.LinearRegression* [Webpage]. [https://scikit-learn.org/stable/modules/generated/sklearn.linear\\_model.LinearRegression.html](https://scikit-learn.org/stable/modules/generated/sklearn.linear_model.LinearRegression.html)

a fixed angle, and a slope that increased linearly with time. The 1st order spatial drift was subtracted using the following steps:

1. Estimate the angle of the positive 1st order drift gradient
2. Estimate the 1st order spatial drift using the found angle
3. Subtract the estimated 1st order spatial drift from the images

Each step is described in detail below. The implementation of 1st order drift correction in Python is shown in Appendix C.3.

### Estimating the angle of the linear gradient

First, the angle of the linear gradient due to 1st order spatial drift was estimated. The angle estimated was the angle along the positive gradient. Listing C.4 shows the Python code estimating the angle.

As the slope of the gradient due to drift increases with time, the gradient is the most visible in the later images. Therefore, the mean of the last ten images was used to estimate the angle of the gradient. The mean image is exemplified in Figure 4.14a. The mean of the last 10 images was used to make the estimate less influenced by noise.

The *Radon transform* from scikit-image<sup>6</sup> was used to estimate the gradient angle in the mean image. The radon transform calculates the projection of an image for a set of angles, and produces a sinogram showing the projection for each degree. The projection of the mean image was calculated for 180 degrees, producing a sinogram as shown in Figure 4.14b.

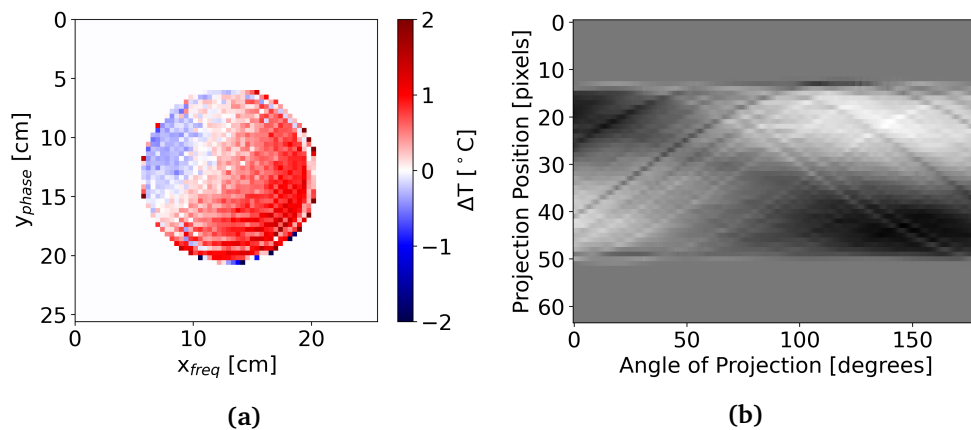


**Figure 4.14:** Sinogram produced from a mean temperature map. (a) The mean temperature map was produced by averaging the last 10 images in a series of temperature maps. (b) The sinogram calculated by applying the Radon transform to the mean temperature map. The sinogram shows the calculated projection for the angles 0-179 degrees.

<sup>6</sup>scikit-image. (2022). *Radon transform* [Webpage]. [https://scikit-image.org/docs/stable/auto\\_examples/transform/plot\\_radon\\_transform.html](https://scikit-image.org/docs/stable/auto_examples/transform/plot_radon_transform.html)

The sinogram was used to find the angle  $\theta$  where the slope of the projected image was greatest, as  $\theta$  will be perpendicular to the angle of the 1st order gradient  $\beta$ . The gradient for every angle was therefore calculated to find the maximum. To do so, the sinogram was first cropped to remove the values outside of the phantom, as shown in Figure 4.15a. The gradient of the projection for each angle was then estimated by using linear regression from scikit-learn. This is illustrated in Figure 4.15b.

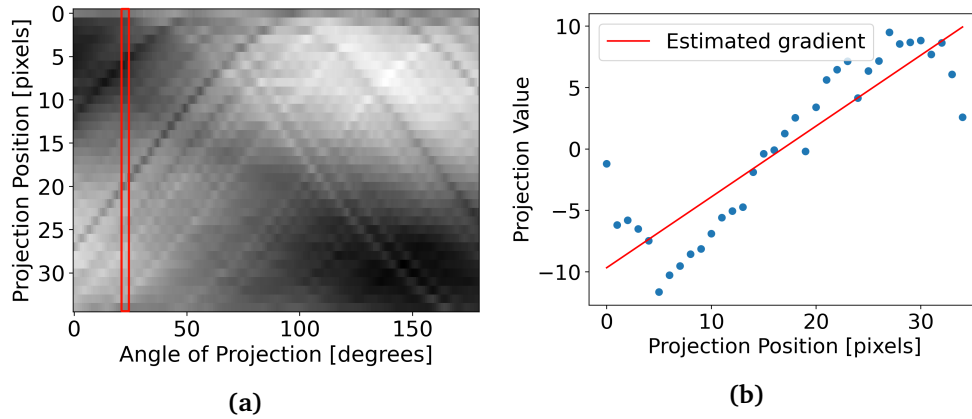


**Figure 4.15:** Estimation of projection gradient. (a) A cropped sinogram. The gradient of the projection was estimated for each angle. (b) Estimation of the projection gradient for a given angle. The plotted data are the projection values from one angle/column in the sinogram in a). Linear regression was used to estimate the gradient for the given angle.

After estimating the gradients by linear regression, each angle of projection had a corresponding gradient slope value.  $\theta$  was found as the angle with the largest absolute value of the gradient slope, as illustrated in Figure 4.16.

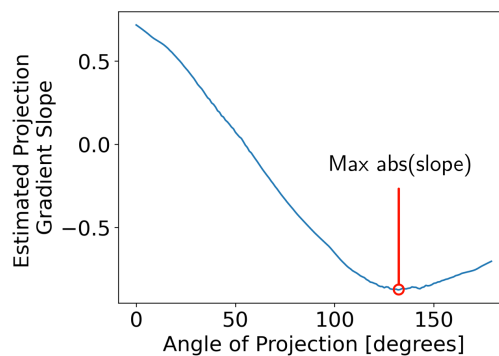


**Figure 4.16:** Finding the angle of projection with maximum slope.

The angle of the positive gradient relative to the positive y-axis ( $\beta$ ) was then found by using  $\theta$  and the sign of the slope. The angle of projection was given

relative to the negative y-axis. The sign of the slope correlated to the direction of the positive gradient. Using this,  $\beta$  was found by Equation 4.5.

$$\beta = \begin{cases} (180 - \theta) - 90 & \text{if slope} \geq 0 \\ (180 - \theta) + 90 & \text{otherwise} \end{cases} \quad (4.5)$$

### Estimating the 1st order spatial drift

Using the estimated angle of the gradient, the 1st order spatial drift was estimated. This was done by calculating the slope of the drift gradient for every image in the sequence of maps, and then estimating the evolution of the slope. It was assumed that the slope of the gradient increased linearly with time, and linear regression was therefore used. The Python implementation is shown in Listing C.5.

First, the slope of the gradient was estimated for all images in the sequence of temperature maps. To do so, the images were first rotated with  $-\beta$  degrees so that the positive gradient was aligned with the positive y-axis. The row-wise mean was then of the pixels that were included by the mask. Resulting was a 1D image of the gradient. This is illustrated in Figure 4.17.

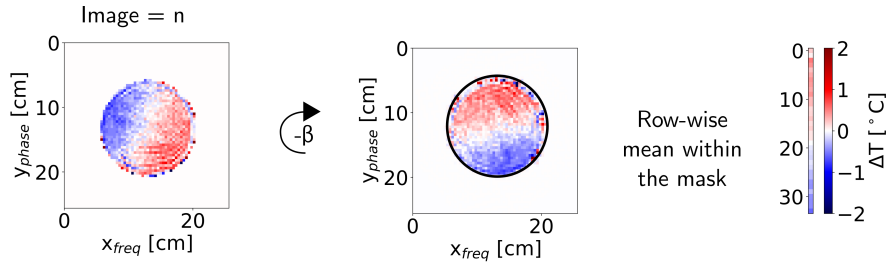


**Figure 4.17:** Producing a 1D image of the gradient from a 2D image. First the 2D images were rotated to align the gradient with the positive y-axis. The row-wise mean within the image mask was then calculated to make the 1D image of the gradient.

After a 1D image of the temperature map was made, the gradient was estimated by using linear regression from scikit-learn. This is shown in Figure 4.18a.

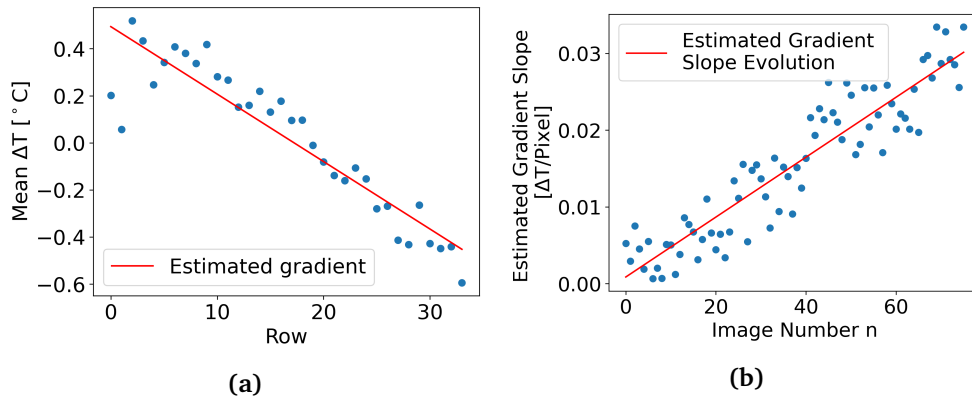


**Figure 4.18:** Estimation of 1st order drift. (a) The gradient of a 1D image as shown in Figure 4.17 was estimated using linear regression. (b) The slope for all images were calculated as shown in Figure a). Linear regression was then used to estimate the evolution of the 1st order drift gradient slope  $A(t_n - t_0)$ .

The gradient was estimated for all images in the sequence of images, and the slope values were logged. Linear regression was then used on slope values from the images to estimate the evolution of the gradient slope  $A(t_n - t_0)$ . This is illustrated in Figure 4.18b.

### Subtracting the spatial 1st order drift from the images

By combining the estimated angle of the linear gradient  $\beta$  and with the estimated slope evolution  $A(t_n - t_0)$ , the 1st order spatial drift  $D_1$  was subtracted from the 0th order corrected images. This was done by making a series of temperature maps of the estimated 1st order drift, and then subtracting them from the 0th order corrected images. The temperature maps of the 1st order spatial drift were made as shown in Figure 4.19.

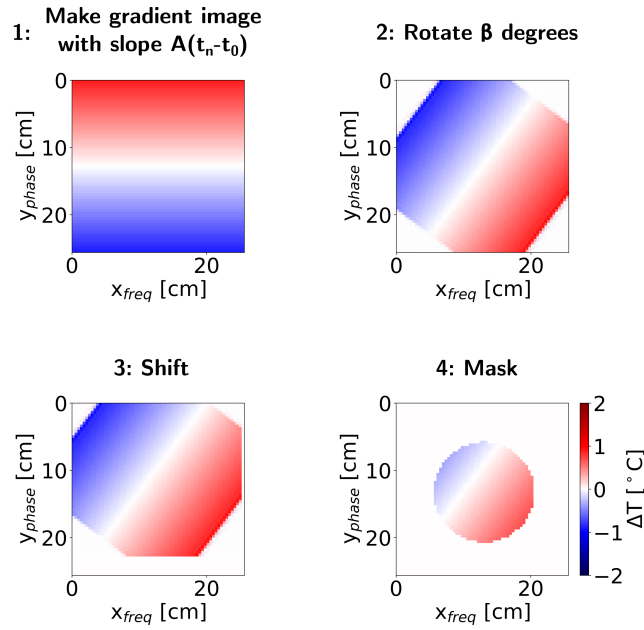


**Figure 4.19:** Making 1st order drift estimate map  $D_1$ . One map was made for every image in the sequence of temperature maps. 1) A gradient image with slope  $A(t_n - t_0)$  was made. 2) The gradient image was rotated by  $\beta$  degrees. 3) The image was shifted so that the gradient value was zero at the location of temperature probe A. 4) The drift image was masked with the same mask used for the sequence of temperature maps.

First a gradient image with slope  $A(t_n - t_0)$  along the positive y-axis was made. The function making the image is shown in Listing C.6. The image was then rotated  $\beta$  degrees by the function in Listing C.7. It was then spatially shifted so that the gradient value was zero at the placement of probe A, as the drift at probe A was removed in the 0th order correction. Finally, the drift map was masked with the same mask used for the temperature maps, see Figure 4.10. The drift maps  $D_1$  were then subtracted from the 0th order drift corrected images, resulting in a sequence of 0th and 1st order drift corrected temperature maps. This is shown in Figure 4.20.

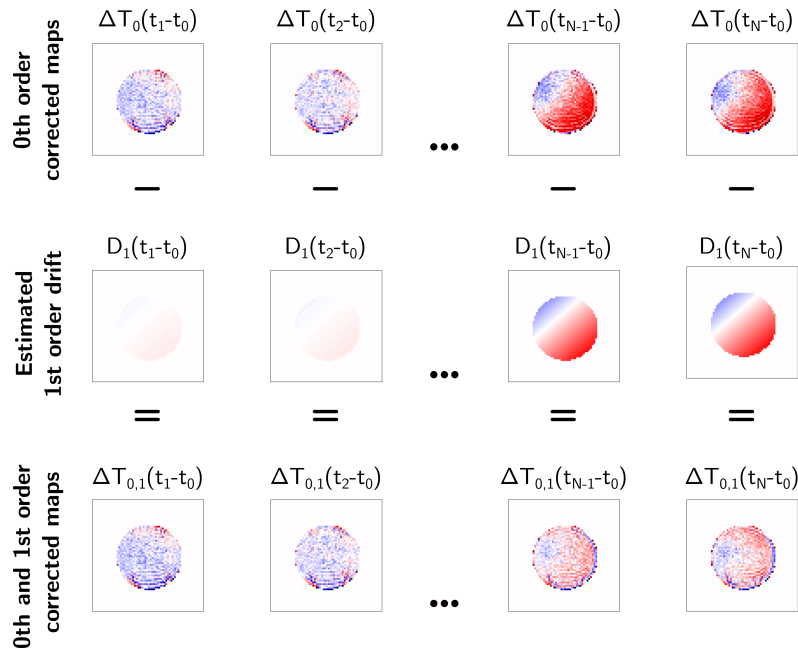


**Figure 4.20:** Subtraction of 1st order drift. The estimated 1st order spatial drift  $D_1(t_n - t_0)$  was subtracted from the 0th order drift corrected images  $\Delta T_1(t_n - t_0)$ . This was done for all images, yielding a sequence of temperature maps corrected for both 0th and 1st order spatial field drift, denoted as  $\Delta T_{0,1}$ .

The subtraction of 1st order spatial drift is shown in Listing C.3.

## 4.8 Experiments

Two runs of experiments were performed to collect data, referred to as Run 1 and Run 2. The experiments were set up to be as identical as possible. One run of experiments was performed as follows. The phantom was brought from a cabinet in the scanner room and placed into the head coil at the patient table. The temperature probes and phantom were then set up as shown in Section 4.1. The head coil and the phantom was placed in the isocenter of the scanner.

After finishing the setup the temperature recording from the Osensa probes were started. The temperature data from the sensors were logged continuously during the experiments. After scanning, the phantom was left in the scanner with the temperature probes. For Run 1 the temperature was logged approximately 9 hours after the last scan. In Run 2 it was recorded for just over two hours after the last scan.

The data from 12 gradient coil temperature sensors on the scanner was logged during and in-between scans. The data was logged manually by taking pictures regularly (approximately every 1-3 minutes) of the computer screen in the controller room. The data was later written to a file.

For both runs of experiments, four image series were acquired. One series consisted of 3 slices with 77 images per slice, as shown in Figure 4.8. Each series was acquired with a different setup of the custom sequence from Section 4.3. The four series of images were acquired using the following order of setups:

1. Standard with minimum SAR (Fat saturation flip angle: 0 degrees).
2. Whisper with minimum SAR (Fat saturation flip angle: 0 degrees).
3. Standard with high SAR (Fat saturation flip angle: 88.5 degrees).
4. Whisper with high SAR (Fat saturation flip angle: 95.2 degrees).

Note that although the exact same setups were used for both runs of experiments, the SAR may differ slightly as the value is calculated at the scanner and depends on previous scans.

It was waited approximately 45 minutes between each acquisition of a series. This was done to let the scanner cool down before a new acquisition, as magnetic field drift is linked to temperature change in the scanner[2].

The image series acquired with the above sequence setups were converted to temperature maps as described in Section 4.5. The temperature maps were 0th order spatial drift corrected as shown in 4.6. The temperature maps were 0th order drift corrected using probe A. Probe B was used purely for evaluation.

The center slices from the Standard sequence setups (setup 1 and 3) were also corrected for 1st order spatial drift as described in Section 4.7. The other series of images were only corrected for 0th order drift as they did not show a 1st order spatial drift gradient, see discussion in Section 6.3. After being 0th and 1st order spatial drift corrected, the center slice images of the Standard series were evaluated.

In addition to the two runs of experiments described above, two experiments were performed to evaluate the accuracy of the OSENSA temperature probes. There was an unexplainable offset in the data, see discussion in Section 6.1. To investigate the readings, the temperature probes were tested in air and water, see Appendix B.1. The probes were also tested in agar gel in Appendix B.2.

## 4.9 Evaluation of the Temperature Maps

The goal was to measure the temperature change due to the RF-induced heating of the imaging sequence itself. To evaluate the method, the measured temperature change in the series of temperature maps was compared to the temperature change measured with the temperature probes. This was done only for the center slice (slice 2) of the Standard series (setup 1 and 3).

For each image in the series the temperature change around probe A and B was estimated by using two 3x3 pixel ROIs around the probe locations in the image. The two ROIs are referred to as ROI A (around probe A) and ROI B (around probe B). The mean pixel values within the ROIs were calculated and plotted with the temperature change measured with probe A and B.

The Root Mean Square Error (RMSE) of the ROI values relative to the probe



data was calculated to evaluate the accuracy of the temperature maps. The RMSE for one series of images was calculated as shown in Equation 4.6.

$$RMSE = \sqrt{\frac{\sum_{n=1}^N (\overline{ROI}(t_n - t_0) - P(t_n - t_0))^2}{N - 1}} \quad (4.6)$$

Here  $\overline{ROI}$  is the mean value from the ROI, and  $P$  is the probe temperature at the same point in time. *numpy.interp* was used to fit the probe data to the time axis of the temperature maps.

## Chapter 5

# Results

This chapter presents the results from the experiments described in Section 4.8. Additional results not included in this chapter can be found in Appendix A.

### 5.1 Session Temperatures

This section presents the session temperatures recorded while running experiments. Figure 5.1 shows the recorded temperature data from the OSENSA probes during the entire session of scanning, for both runs of experiments.

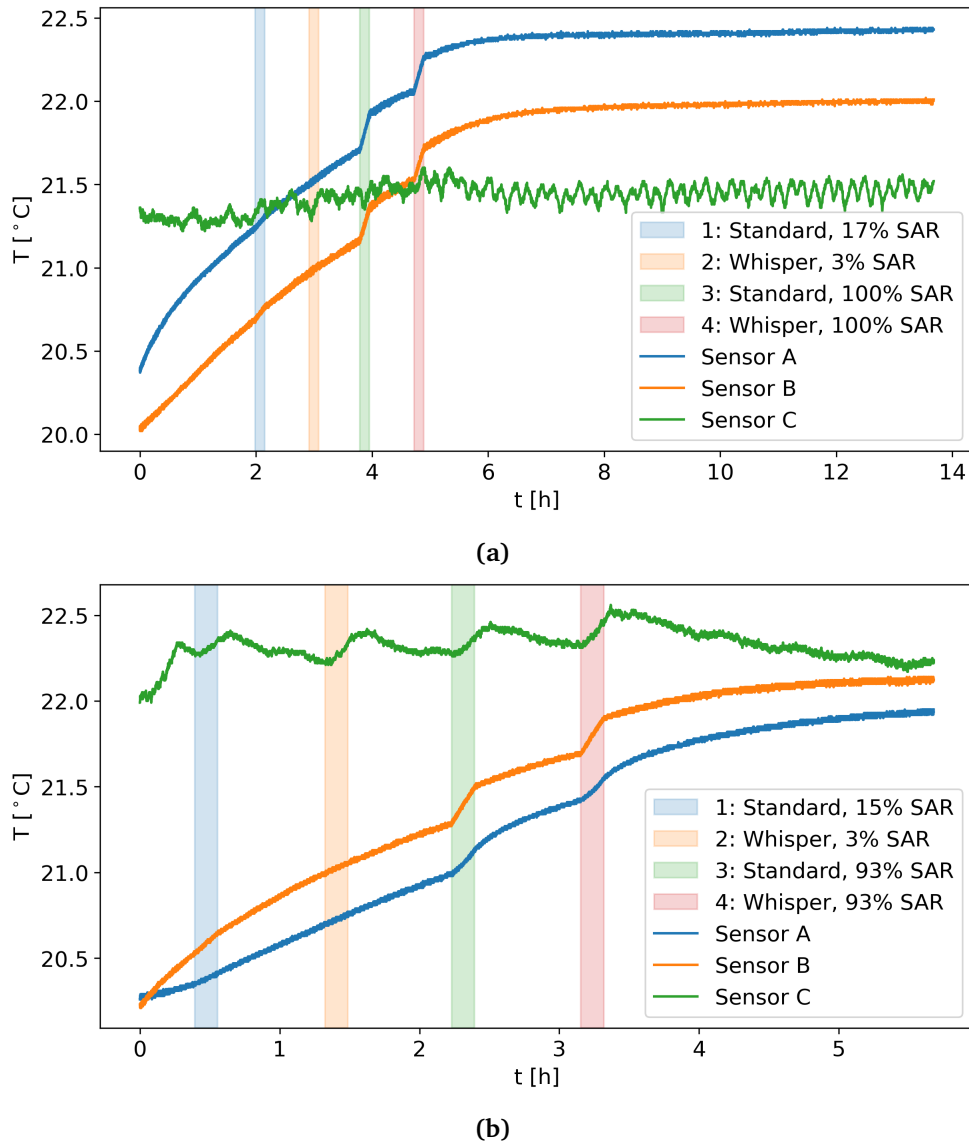


**Figure 5.1:** Session temperature data. (a) Run 1. (b) Run 2. The plots show the recorded temperature from probe A, B and C. Probe A and B were placed in the agar phantom, while probe C was placed in the air just outside of the phantom. The probe placement is shown in Section 4.1. The colored areas show when the four series of images were acquired. A new series was acquired approximately 45 minutes after the previous ended so that the scanner could cool down.

Seen in Figure 5.1a, the data indicate that the temperatures at probe A, B and C stabilize at different temperatures. This is discussed in Section 6.1. Due to these measurements, two experiments were performed to evaluate the probes, see Appendix B. The first experiment validated the accuracy of the probes in air and water, and confirmed the  $\pm 0.1^\circ\text{C}$  accuracy. The second experiment tested

the probes in the agar gel. The experiment was not carried out long enough to see if the temperatures stabilized at  $\pm 0.1^\circ\text{C}$ , and could therefore not provide any answers to the strange results.

The mean gradient system temperatures during and in-between acquisitions are plotted for both runs of experiments in Figure 5.2. The mean was taken of 12 gradient coil temperature sensors.

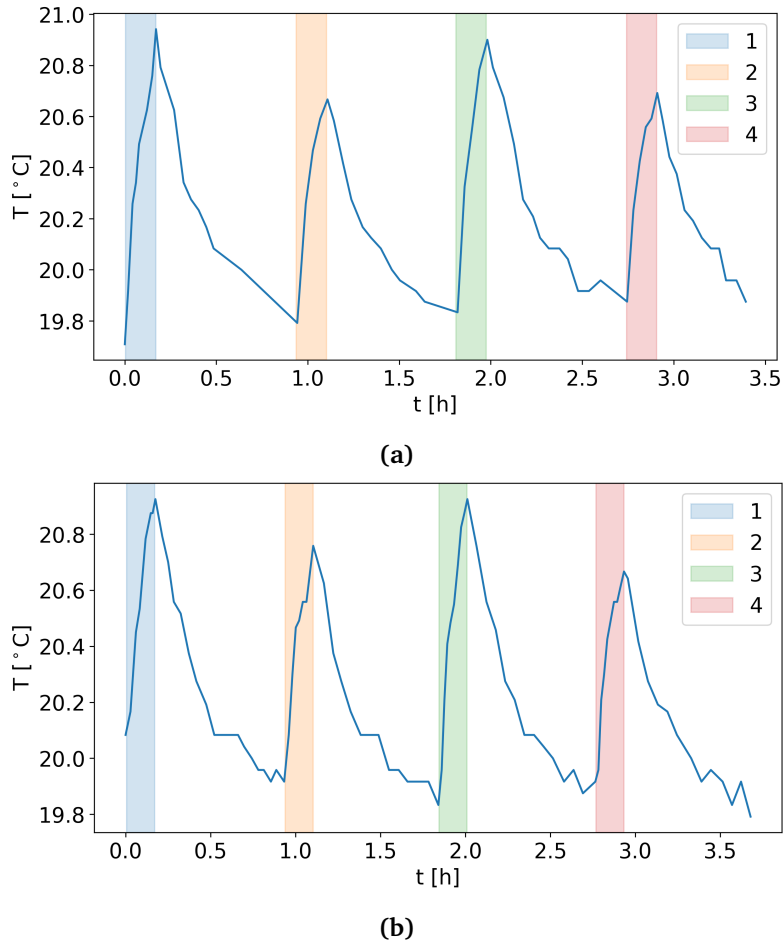


**Figure 5.2:** Mean gradient system temperatures during and in-between acquisitions. (a) Run 1. (b) Run 2. The mean is calculated from 12 gradient coil temperature sensors. The colored areas show when the four series of images, as described in Section 4.8, was acquired.

## 5.2 Drift Correction

The results of the drift corrections are shown in this section. For each series, the last temperature map from each slice is presented. The last maps show the measured temperature change due to RF-induced heating after acquiring the image

series. The acquisition of one image series lasted 10 minutes.

First, the raw temperature maps from Run 1 without any drift correction are presented in Figure 5.3.

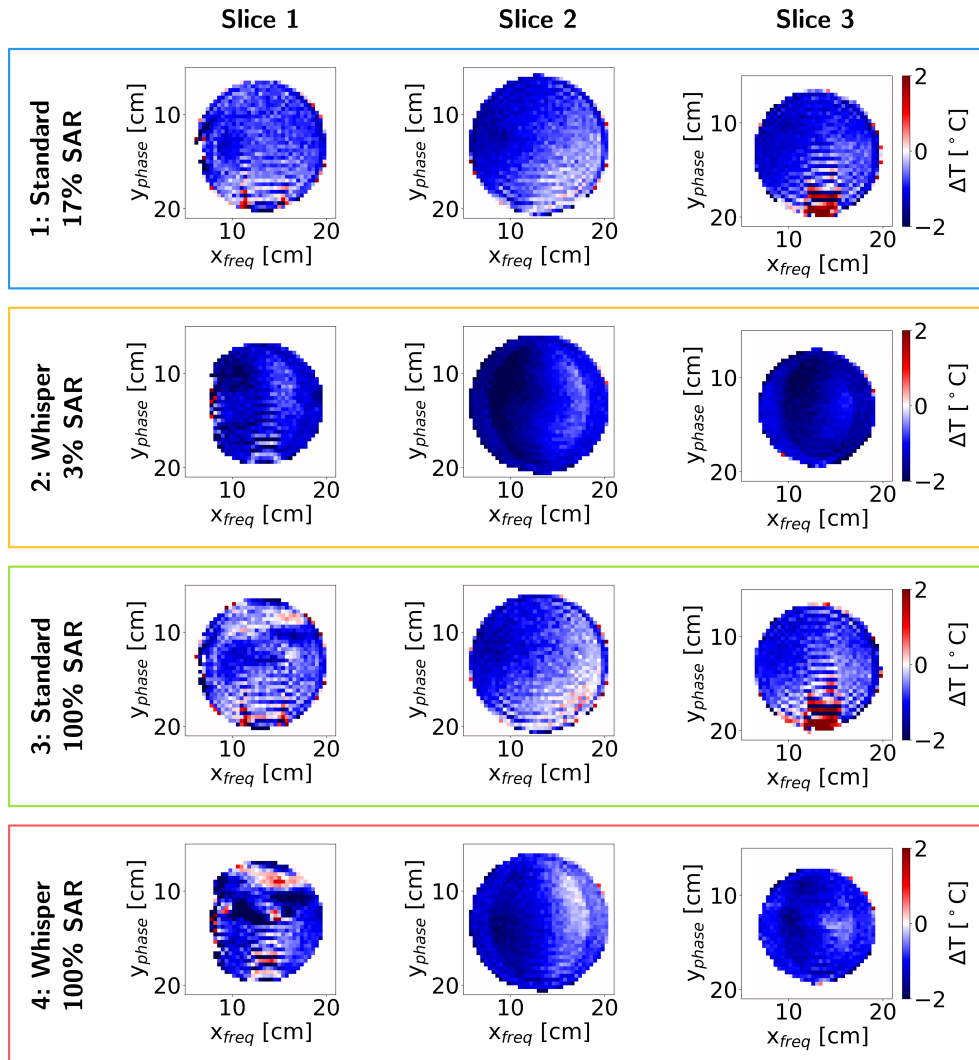


**Figure 5.3:** Raw temperature maps from Run 1. The figure displays the last temperature map from all slices (1-3) and series (1-4). The last image shows the measured temperature change after acquiring the entire image series (10 minutes).

The images from Run 2 were similar and can be viewed in Figure A.1 in Appendix A.

The estimated 0th order spatial drifts from Run 1 are shown in Table 5.1.

**Table 5.1:** Estimated 0th order spatial drift for each series in Run 1. The values are the estimated 0th order spatial drift after the 10 minutes of acquisition for each series.

	Slice 1 [°C]	Slice 2 [°C]	Slice 3 [°C]
1: Standard, 17% SAR	-1.01	-1.14	-1.28
2: Whisper, 3% SAR	-1.45	-1.67	-1.75
3: Standard, 100% SAR	-1.04	-1.23	-1.24
4: Whisper, 100% SAR	-1.31	-1.50	-1.55

The estimated 0th order spatial drifts from Run 2 are shown in Table Table 5.2.

**Table 5.2:** Estimated 0th order spatial drift for each series in Run 2. The values are the 0th order spatial drift after the 10 minutes of acquisition for each series.

	Slice 1 [°C]	Slice 2 [°C]	Slice 3 [°C]
1: Standard, 15% SAR	-1.02	-1.23	-1.34
2: Whisper, 3% SAR	-1.52	-1.69	-1.78
3: Standard, 93% SAR	-1.00	-1.25	-1.29
4: Whisper, 93% SAR	-1.35	-1.55	-1.56

The 0th order spatial drift was subtracted from the images. Figure 5.4 shows the 0th order drift corrected temperature maps from Figure 5.3. The 0th order drift corrected images from Run 2 are shown in Figure A.2.

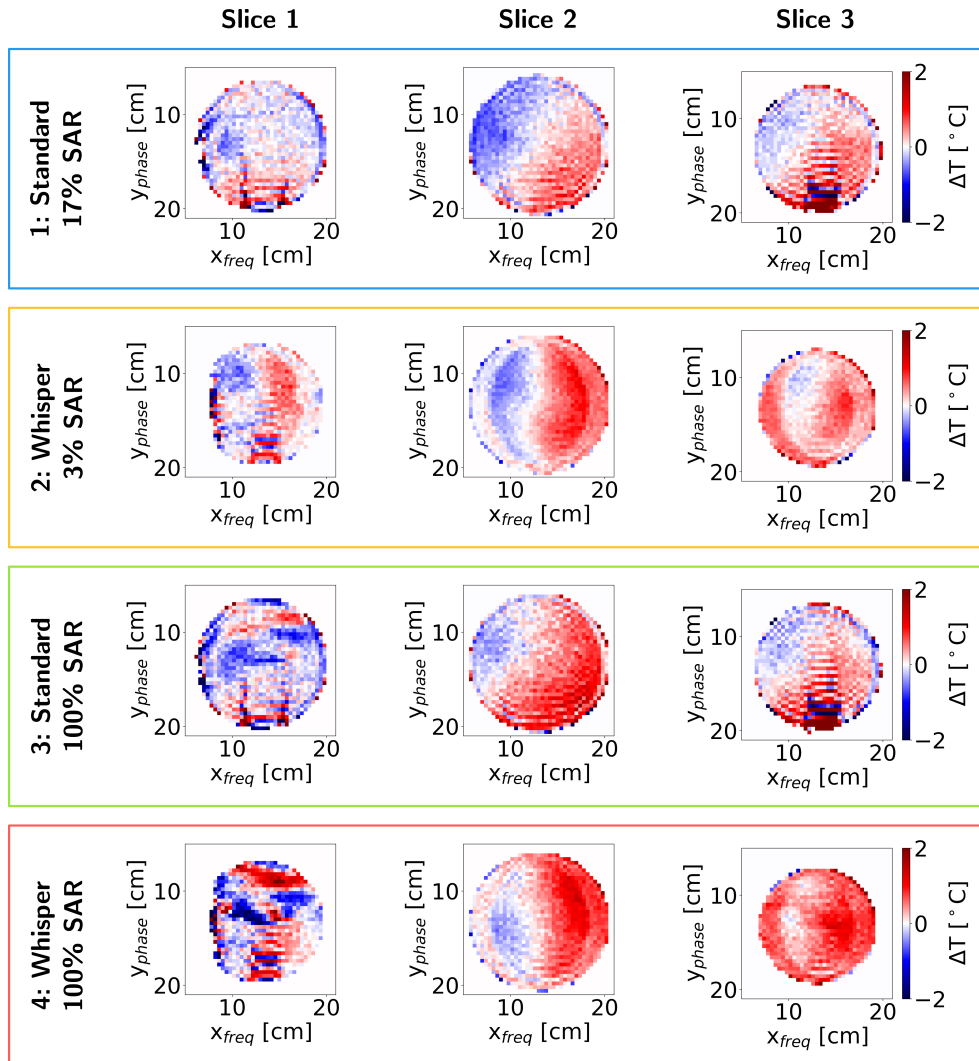


**Figure 5.4:** 0th order drift corrected temperature maps from Run 1. The figure displays the last 0th order drift corrected temperature map from all slices (1-3) and series (1-4). The last image shows the measured temperature change after acquiring the entire image series (10 minutes).

The images from slice 2 in the Standard series (series 1 and 3) were corrected for both 0th and 1st order spatial field drift. The estimated slopes of the 1st order spatial gradient are shown in Table 5.3.

**Table 5.3:** Estimated gradient slopes due to 1st order spatial drift. The slopes values are the estimated slopes for the last image in the series, i.e. the estimated drift gradient slope after the 10 minutes of acquisition. The angle is illustrated for each series in Figure 5.5a and A.3a.

	Run 1 [ $^{\circ}\text{C}/\text{cm}$ ]	Run 2 [ $^{\circ}\text{C}/\text{cm}$ ]
1: Standard, Low SAR	0.08	0.11
3: Standard, High SAR	0.09	0.12

The last 0th and 1st order spatial drift corrected temperature maps from the Standard sequences from Run 1 are shown in Figure 5.5.

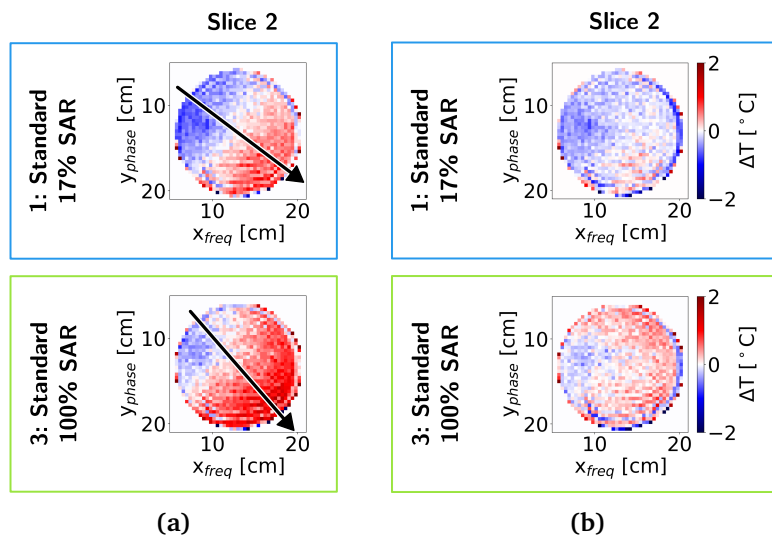


**Figure 5.5:** (a) The last 0th order drift corrected images from Run 1. The arrow shows the estimated direction of the positive gradient in the 1st order spatial drift. (b) 0th and 1st order drift corrected images from Run 1. Only the images from slice 2 in the Standard series were corrected for both 0th and 1st order drift. This figure shows the last corrected temperature maps from slice 2 in the Standard series. The map shows the estimated temperature change after acquiring the entire image series (10 minutes).

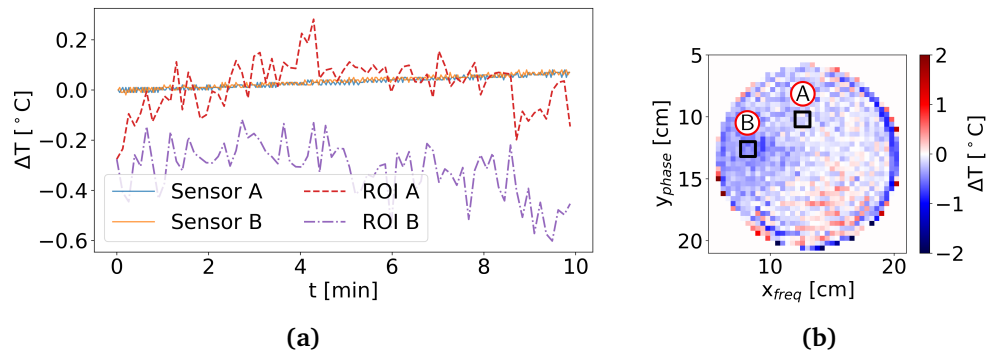
The images from Run 2 are shown in Figure A.3.

### 5.3 Temperature Map Evaluation

The 0th and 1st order spatial drift corrected temperature maps from slice 2 in the Standard series (Figure 5.5 and A.3) were evaluated on their performance against the OSENSA temperature probes, as described in Section 4.9.

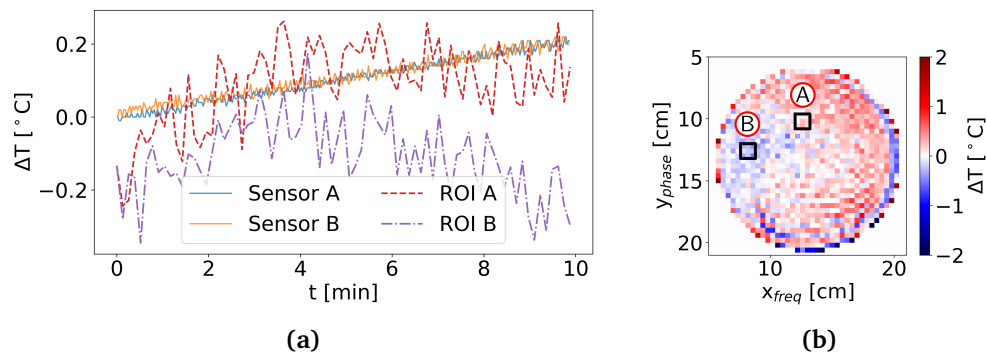
Figure 5.6 shows the plotted ROI temperatures from 1: Standard series with low SAR (slice 2, Run 1) along with the probe data.





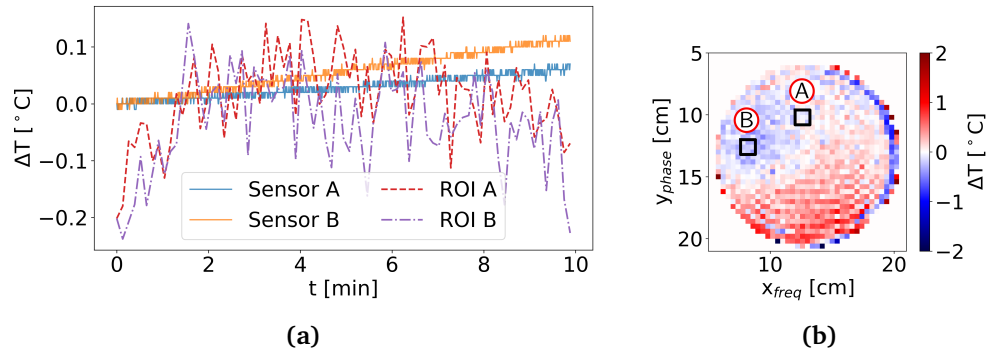
**Figure 5.6:** (a) The ROI temperatures from 1: *Standard series with low SAR* (slice 2, Run 1) plotted with the probe data. The SAR of the series was calculated to be 17%. The ROIs were placed as shown in Figure b). Each ROI value is the mean pixel value within the ROI from the image at time  $t$ , i.e there are two ROI values (A and B) per temperature map in the sequence of images. The RMSE value between ROI A and probe A was  $0.10^{\circ}\text{C}$ . Between ROI B and probe B, the RMSE was  $0.37^{\circ}\text{C}$ . (b) The last temperature map in the series showing ROI A and ROI B. The ROIs are centered around the placement of the probes, which can be seen in Figure 4.4c.

Figure 5.7 shows the plotted ROI temperatures from 3: *Standard series with high SAR* (slice 2, Run 1) along with the probe data.



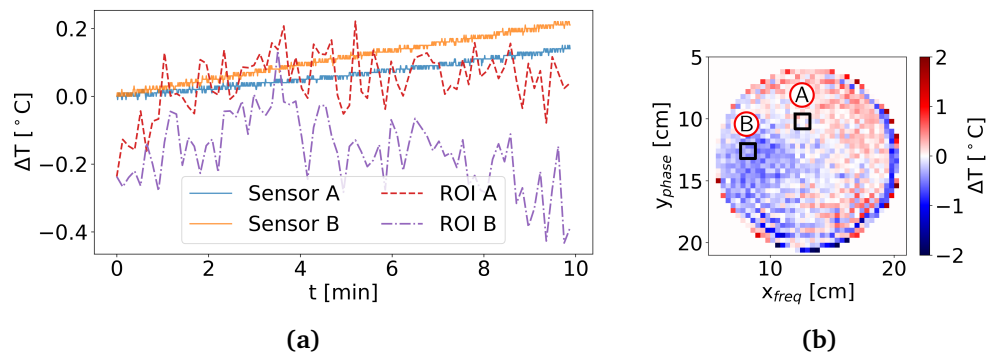
**Figure 5.7:** (a) The ROI temperatures from 3: *Standard series with high SAR* (slice 2, Run 1) plotted with the probe data. The SAR of the series was calculated to be 17%. The ROIs were placed as shown in Figure b). Each ROI value is the mean pixel value within the ROI from the image at time  $t$ , i.e there are two ROI values (A and B) per temperature map in the sequence of images. The RMSE value between ROI A and probe A was  $0.10^{\circ}\text{C}$ . Between ROI B and probe B, the RMSE was  $0.25^{\circ}\text{C}$ . (b) The last temperature map in the series showing ROI A and ROI B. The ROIs are centered around the placement of the probes, which can be seen in Figure 4.4c.

Figure 5.8 shows the plotted ROI temperatures from 1: *Standard series with low SAR* (slice 2, Run 2) along with the probe data.



**Figure 5.8:** (a) The ROI temperatures from 1: *Standard series with low SAR* (slice 2, Run 2) plotted with the probe data. The SAR of the series was calculated to be 15%. The ROIs were placed as shown in Figure b). Each ROI value is the mean pixel value within the ROI from the image at time  $t$ , i.e there are two ROI values (A and B) per temperature map in the sequence of images. The RMSE value between ROI A and probe A was  $0.08^{\circ}\text{C}$ . Between ROI B and probe B, the RMSE was  $0.12^{\circ}\text{C}$ . (b) The last temperature map in the series showing ROI A and ROI B. The ROIs are centered around the placement of the probes, which can be seen in Figure 4.4c.

Figure 5.8 shows the plotted ROI temperatures from 3: *Standard series with high SAR* (slice 2, Run 2) along with the probe data.



**Figure 5.9:** (a) The ROI temperatures from 3: *Standard series with high SAR* (slice 2, Run 2) plotted with the probe data. The SAR of the series was calculated to be 93%. The ROIs were placed as shown in Figure b). Each ROI value is the mean pixel value within the ROI from the image at time  $t$ , i.e there are two ROI values (A and B) per temperature map in the sequence of images. The RMSE value between ROI A and probe A was  $0.08^{\circ}\text{C}$ . Between ROI B and probe B, the RMSE was  $0.31^{\circ}\text{C}$ . (b) The last temperature map in the series showing ROI A and ROI B. The ROIs are centered around the placement of the probes, which can be seen in Figure 4.4c.

The RMSE values from the Standard series from both runs of experiments are summarized in Table 5.4.

**Table 5.4:** RMSE values. The RMSE values were calculated using Equation 4.6, and is a measure of the error between ROIs and the temperature probes used as ground truth. The ROIs are illustrated in Figure 5.9b.

Sequence	RMSE A [ $^{\circ}$ C]	RMSE B [ $^{\circ}$ C]
Run 1: Standard, 17% SAR	0.10	0.37
Run 1: Standard, 100% SAR	0.10	0.25
Run 2: Standard, 15% SAR	0.08	0.12
Run 2: Standard, 93% SAR	0.08	0.31

## 5.4 Oscillating Temperature

Image series with high SAR (series 3 and 4) showed an oscillating drift in slice 1. To illustrate this, the ROI mean from three ROIs were plotted for 3: *Whisper series with high SAR* from Run 1. The plot is shown in Figure 5.10.

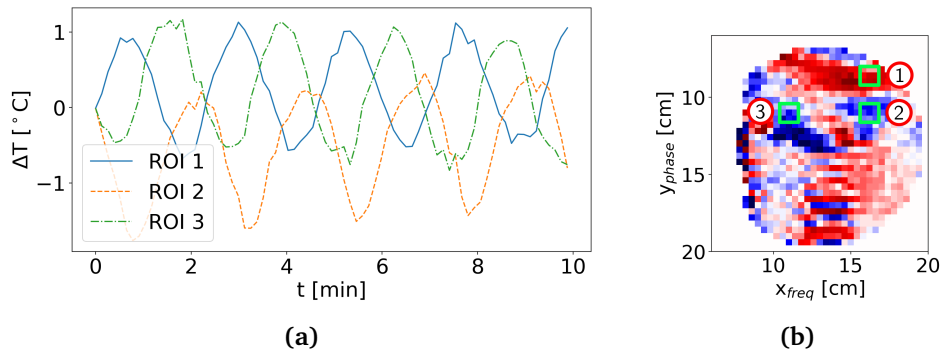


**Figure 5.10:** Oscillating drift in high SAR series. Series 4: *Whisper with high SAR* from Run 1 was used to make the plot. The plot shows the ROI temperature from three ROIs. (b) The placement of the ROIs used to make the plot in a).

## Chapter 6

# Discussion

In this chapter, the results from Chapter 5 are discussed. The chapter is divided into sections discussing different results and their implications.

### 6.1 Session Temperatures and the Probe's Reliability

The full session temperature data in Figure 5.1 indicate that the phantom was 1-2°C cooler than the air in the scanner, even though it was kept in a cabinet in the scanner room. At once the phantom was placed in the scanner, the temperature started increasing. Ideally, it should have been placed in the scanner hours before starting the acquisitions so that it could reach thermal equilibrium before scanning. This was however difficult to achieve due to limited time at the scanner. Although the temperature was increasing even without inputting RF energy, the increase while scanning was noticeable. Especially for the high SAR sequences where the phantom temperature increased  $\approx 0.2^\circ\text{C}$ .

According to the OSENSA temperature probe data from Run 1 of experiments, the phantom temperature increased above the temperature of the air surrounding it. See Figure 5.1a. The temperature at probe A stabilized at  $\approx 22.5^\circ\text{C}$ , probe B at  $\approx 22^\circ\text{C}$  and the air temperature from probe C at  $\approx 21.5^\circ\text{C}$ . The results indicate a stable temperature gradient in the phantom at thermal equilibrium, breaking with the second law of thermodynamics. It was therefore evident that something was wrong with the temperature measurements. The offsets between the data from the probes were also seen in Run 2 (Figure 5.1b), but not to the same extent. The data was not recorded long enough for the temperature to stabilize in Run 2.

The experiments in Appendix B evaluating the probes did not provide any answers to the strange readings. The first experiment in Appendix B.1 confirmed the accuracy of the probes in air and water. The agar experiment in Appendix B.2 was not performed for long enough, which means the agar gel could still be the source. One possibility is a chemical reaction due to the agar gel. If so, the chemical reaction had to be very stable over time, which might not be realistic. The reason for the strange temperature readings remains a mystery, and should be investigated further.

The temperature evolution at probe A and B in Figure 5.1a did however seem to follow a similar path, only with an offset between them. As only temperature change is measurable with PRF shift thermometry, the absolute temperature was of limited importance. Therefore, no more effort was put into investigations of the temperature sensors for this project. Despite the unusual readings, the temperature change measured with the probes were used for evaluation of the temperature maps.

## 6.2 Gradient System Temperatures and Reproducibility

The similarity between the gradient system temperatures in Figure 5.2 verifies the similarity of the two runs of experiments, which is important when assessing the reproducibility of the results. As discussed in Section 3.5, the temperature of the scanner is linked to the magnetic field drift.

In Run 2 of experiments, the starting mean gradient system temperature was  $\approx 0.4^\circ\text{C}$  higher than in Run 1, which may result from previous scanning and not waiting long enough before starting the acquisition of series 1. Despite the different starting points, the temperature evolution in both runs of experiments followed approximately the same path. This verifies the quality of the two runs of experiments, and that the results from both runs of experiments should be comparable.

The comparability of the two runs was further confirmed by the temperature maps. When visually comparing the 0th order spatial drift corrected maps from Run 1 and Run 2, seen in Figure 5.4 and A.2 respectively, they look very similar. This indicates that the drift is reproducible, which is beneficial in characterizing and removing it.

The magnitude of the spatial 0th order drift was very similar between the two runs, see Table 5.1 and 5.2. The drift in all series and slices ranged from  $-1.7^\circ\text{C}$  to  $-1.01^\circ\text{C}$ . In a previous project by the author[4], the scanner was not cooled down before the start of each new acquisition. The 0th order drift then ranged from  $-1^\circ\text{C}$  to  $5^\circ\text{C}$  after 12 minutes of scanning. Table 5.1 and 5.2 also reveals that the 0th order spatial drift from the same slice and series was very similar between Run 1 and 2. The difference between the two runs was less than  $0.1^\circ\text{C}$  for all series and slices, further confirming the reproducibility of the results. Tables 5.1 and 5.2 also indicate that the magnitude of 0th order drift was larger for the Whisper series, as well as increasing from slice 1 to 3.

The 1st order drift also seemed to be reproducible. As shown in Table 5.3, the slopes of the 1st order spatial gradients were roughly the same between Run 1 and 2, differing with only  $0.03^\circ\text{C}/\text{cm}$  for both the high and low SAR Standard series. The reproducible drift was likely linked to the gradient system being cooled down before the start of each new scan.

The plots of the gradients in Figure 5.2 show that the system heats less when using the Whisper gradient mode. This is to be expected as the gradient rise times are increased. As drift is linked to scanner temperature increase, the Whisper

series should show less drift as the scanner is heated less. This is however the opposite of what was seen in Table 5.1 and 5.2, where the drift appeared to be larger for the Whisper series. This shows that looking only at the gradient system temperature is likely too simple to fully describe the drift.

### 6.3 Temperature Maps and Drift Correction

The raw temperature maps in Figure 5.3 and A.1 were all dominated by 0th order drift. After correcting for the 0th order drift, the spatial variations became more visible, see Figure 5.4 and A.2. Slice 1 in all the 0th order corrected image series revealed spatial variations of orders larger than 2, and was therefore deemed unusable. This could be due to imperfect shimming or other factors. For the high SAR series, slice 1 showed a sinusoidal and oscillating drift. This is further discussed in 6.4.

Slice 2 (in the isocenter of the scanner) showed the most promising results. The Standard series had a linear gradient as expected. The Whisper series also seemed to have a gradient, but with some artifact near the edge of the phantom in the frequency encoding direction. The artifact could be connected to the lower gradient performance in Whisper mode (due to increased rise time), but the exact reason remains unclear. The Whisper sequence was therefore also considered as unusable. The images from slice 3 seemed similar to those from slice 2, but more noisy and therefore not used either. Only the images from slice 2 in the Standard series were corrected from 1st order drift.

By visual inspection, the 0th and 1st order corrected Standard images seemed to possess 2nd order drift. See Figure 5.5 and A.3. In the middle left of the phantom the maps show a "cold spot". Due to the shorter wavelength at 7T ( $\approx 11$ cm in the phantom), inhomogeneous heating could occur. The plotted probe temperatures in Figure 5.8 and 5.9 show that the temperature at probe B actually increased faster at probe B than at probe A, suggesting inhomogeneous heating. But as the difference was only seen in Run 2, and the probes showed strange behaviour (as discussed in Section 6.1), it should not be taken as definite proof of inhomogeneous heating. It did however seem like there was inhomogeneous heating.

The inhomogeneous heating read by the probes in Run 2 did not match with the temperature maps. In the temperature maps the 'cold spot' indicated that the temperature at probe B was lower than at probe A, and decreasing. Whether there was inhomogeneous heating or not, the temperature should be increasing. This further indicates that the "cold spot" was 2nd order drift. 2nd order drift is harder to estimate and remove by estimating it like the 1st order drift, as there is a possibility that it is actual temperature change.

The same can be said about the 1st order drift correction from Section 4.6. The linear gradient across the image was assumed to be purely 1st order spatial magnetic field drift. If the heating was anything but perfectly homogeneous, it would be included in the 1st order drift estimation and introduce errors. But as the gradient across the images after 10 minutes was at the order of 1-2°, while

the actual measured temperature increase was 0.1-0.2°C, it can be argued that the actual increase would not affect the estimate greatly. Ideally, three temperature sensors should have been used to estimate the 1st order drift.

Masking away all noisy and bad pixels was challenging, and remaining pixels influence the results. As seen in the temperature maps in Figure 5.5, several pixels along the edge of the phantom showed extreme values that most likely were not due to actual temperature change. This may negatively affect the estimated gradient angle and slopes. Resulting could be spatial varying errors (due to incorrect estimated angle) and time varying errors (due to incorrect estimated slope evolution). The apparent 2nd order spatial drift in Figure 5.5 could therefore also be due to an inaccurate angle estimate. The 0th order spatial drift corrected images in Figure 5.4 did however seem to have the same "cold spot", indicating that it was 2nd order spatial drift.

## 6.4 Performance

For the method to be usable, one should be able to control that the temperature increase does not exceed 1°C at any position in the phantom. The target accuracy was therefore set to 0.1° at all spatial positions. As seen in Table 5.4, the RMSE at the location of temperature probe A was 0.08-0.10°C. Probe A was however used for the 0th order drift correction, and is therefore not representative of the actual accuracy. It can however be seen as a "best case".

Probe B was used for evaluation only, and the RMSE revealed a significantly lower accuracy. As shown by Table 5.4, the RMSE ranged from 0.12-0.37°C, while the actual heating measured with the probes during the acquisitions was  $\approx$ 0.1-0.2°C. The RMSE from probe B indicates that the accuracy of the PRF thermometry method in this report is too low to be used for validation of SAR simulations. Alternatively, a safety margin could be added to the measurements. But the larger the safety margin has to be, the less useful the method is. As an RMSE of 0.37° was observed, the safety margin would have to be relatively high compared to the maximum tolerated temperature increase of 1°C.

The calculated RMSE values will however be prone to placement errors of the probes. Although the probes can be located in the transversal magnitude images (x- and y-location), the tip of the probes were likely not placed exactly in the slice 2's location along the z-direction. This results in an error in the RMSE values.

Although the RMSE values may be affected by placement errors, the plotted temperatures from ROI B in Figure 5.7 further arguments for the inaccuracy of the estimated temperature change. The temperature seemingly increases before starting to decrease again. This while probe B shows a steady increase. The decrease is likely linked to 2nd order spatial drift, as discussed in Section 6.3. As discussed in Section 6.2, the drift seemed to be reproducible. By acquiring more images and placing the probes at different the locations, the drift could perhaps be characterised, modelled and removed to obtain better estimates.

Filtering the raw temperature data could also improve the accuracy of the

method. As seen in the ROI plots in figures 5.6 - 5.9, the temperature estimates are rapidly fluctuating. Based on these results, it seems like the accuracy could be improved by filtering the data. This could be done either by simply averaging, or use statistical methods such as Kalman filtering. It could be applied in the spatial dimensions as the temperature maps realistically should be somewhat smooth. It could also be applied along time as it is limited how much the temperature can fluctuate given the inputted energy and realistic heat transportation.

The accuracy discussed in this section is only for the center slice (slice 2). The slice is only 4mm thick, and thus the temperature change of the rest of the phantom is unknown. The value of the method is further limited if only one slice can be observed.

Sequences with high and low SAR were applied to evaluate the method. Based on the four RMSE values from ROI B in Table 5.4, one can not conclude that there is a difference in accuracy due to SAR. More experiments should be performed to find out if the heating affects the RMSE.

## 6.5 Oscillating Temperature

The plotted ROI temperatures in Figure 5.10 show an apparent oscillating temperature change/magnetic field drift with amplitude 0.5-1°C, which is not described in any literature. The oscillation was visible at some local hot spots, but with a phase difference between them. The period of the oscillation was just above 2 minutes, which is a much larger timescale than a sequence ( $TR = 60ms$ ). The source of the oscillations remains unknown. At the time the experiments were performed there was an error with the RF at the scanner, but it is unclear whether this could be the reason for the oscillations.

Although the oscillating noise was most prominent in slice 1, it could still be present to a smaller degree in the other slices. Further efforts should therefore be spent on identifying the source of the oscillations.



## Chapter 7

# Conclusion and Future Work

### 7.1 Conclusion

The aim of this thesis was to investigate whether PRF shift thermometry could be used to measure RF-induced heating due to the thermometry imaging sequence itself, using a temperature probe for 0th and 1st order drift correction. The targeted accuracy was set to  $0.1^{\circ}\text{C}$  across the temperature maps. If the PRF shift thermometry could deliver such an accuracy, it could be valuable in verification of new transmit coils for use in MRI.

The PRF shift thermometry was implemented at a 7T Siemens MAGNETOM Terra scanner at St. Olav's University Hospital, along with a 1Tx/32Rx head coil. The experiments were performed at an agar phantom made specifically for this project. A customized Gradient Recalled Echo sequence with added SAR control was used to acquire the images. Series of 77 images were acquired for 10 minutes to measure the RF-induced heating resulting from the imaging sequence itself. The image series were then converted to temperature maps. Only the image series from slice 1 in the Standard series revealed to be usable. They were corrected for 0th and 1st order drift, and the temperature maps were evaluated both visually and against temperature probes. Two probes inserted in the phantom were used in the evaluation. One had already been used for correction of magnetic field drift, while the other was used purely for evaluation. The temperature increase at the probe locations was estimated by averaging over 9 pixel ROIs in the temperature maps. The ROI values were compared to the probe data.

During the 10 minutes long acquisitions, the RF-induced heating of the phantom was in the range  $0.1\text{-}0.2^{\circ}\text{C}$ , depending on the SAR of the sequence. At the position of the probe used for drift correction, the temperature map delivered an RMSE of  $\approx 0.1^{\circ}\text{C}$ , as shown in Table 5.4. The temperature maps did however reveal what was most probably 2nd order drift in the phantom, see Figure 5.5. The drift affected the temperature estimates negatively, and the RMSE values at the probe used purely for evaluation ranged from  $0.12\text{-}0.37^{\circ}\text{C}$  (Table 5.4). The drift did however seem reproducible, which can be seen by comparing Figure 5.4 and A.2. This was likely due to letting the scanner cool down before starting the acquisition

of a new image series.

Some strange results were also seen in this report. The temperature sensors in the phantom stabilized at an apparent temperature gradient (see Figure 5.1a), which breaks with the laws of physics. One of the edge slices in the high SAR series also showed an apparent oscillating temperature change with a period of approximately 2 minutes, see Figure 5.10. The source of these strange results was not identified, and should be further investigated.

In summary, the accuracy of the temperature measurements at the probe used for validation was too low, revealing an RMSE value ranging from 0.12-0.37°C. This was likely due to 2nd order spatial field drift. The drift seemed reproducible, which means it could be possible to remove it to acquire better estimates. However, the PRF shift thermometry method proposed in this thesis was not accurate enough to measure the RF-induced heating of a phantom due to the thermometry sequence itself.

## 7.2 Future Work

More experiments should be done to further examine the reproducibility of the the drift and temperature maps. This should be done to see if the 2nd order spatial drift could be removed somehow. In this report, only two sets of acquisition parameters were used. It may be possible to optimize the acquisition parameters to obtain the best result. Further work should also be put into improving the temperature map accuracy by filtering both in the spatial and temporal domain. The temperature probes should also be tested further to find the source of the strange temperature readings. Finally, the root of the oscillating drift should be identified as the oscillation reduces the credibility of the results.

# Bibliography

- [1] P. C. Lauterbur, 'Image formation by induced local interactions: Examples employing nuclear magnetic resonance,' *Nature*, vol. 242, no. 5394, pp. 190–191, 1973, ISSN: 1476-4687. DOI: 10.1038/242190a0. [Online]. Available: <https://doi.org/10.1038/242190a0>.
- [2] C. Bing, R. M. Staruch, M. Tillander, M. O. Köhler, C. Mougenot, M. Ylihautila, T. W. Laetsch and R. Chopra, 'Drift correction for accurate prf-shift mr thermometry during mild hyperthermia treatments with mr-hifu,' *International journal of hyperthermia : the official journal of European Society for Hyperthermic Oncology, North American Hyperthermia Group*, vol. 32, no. 6, pp. 673–687, 2016, 27210733[pmid] PMC5045807[pmcid], ISSN: 1464-5157 0265-6736. DOI: 10.1080/02656736.2016.1179799. [Online]. Available: <https://pubmed.ncbi.nlm.nih.gov/27210733/> <https://www.ncbi.nlm.nih.gov/pmc/articles/PMC5045807/>.
- [3] P. Ehse, F. Fidler, P. Nordbeck, E. D. Pracht, M. Warmuth, P. M. Jakob and W. R. Bauer, 'Mri thermometry: Fast mapping of rf-induced heating along conductive wires,' *Magn Reson Med*, vol. 60, no. 2, pp. 457–61, 2008, 1522-2594 Ehse, Philipp Fidler, Florian Nordbeck, Peter Pracht, Eberhard D Warmuth, Marcus Jakob, Peter M Bauer, Wolfgang R Journal Article Research Support, Non-U.S. Gov't United States Magn Reson Med. 2008 Aug;60(2):457-61. doi: 10.1002/mrm.21417., ISSN: 0740-3194. DOI: 10.1002/mrm.21417.
- [4] C. F. Haakonsen, 'Mr thermometry of phantoms using water proton chemical shift,' Department of Electronic Systems, NTNU – Norwegian University of Science and Technology, Project report in TFE4580, Dec. 2021.
- [5] P. C. Liang Zhi-Pei; Lauterbur, *Principles of Magnetic Resonance Imaging - A Signal Processing Perspective*, ser. IEEE Press Series in Biomedical Engineering. New York: IEEE Press Marketing, 2000, ISBN: 0-7803-4723-4.
- [6] I. Grässlin, H. Homann, S. Biederer, P. Börner, K. Nehrke, P. Vernickel, G. Mens, P. Harvey and U. Katscher, 'A specific absorption rate prediction concept for parallel transmission mr,' *Magnetic resonance in medicine : official journal of the Society of Magnetic Resonance in Medicine / Society of Magnetic Resonance in Medicine*, vol. 68, pp. 1664–74, 2012. DOI: 10.1002/mrm.24138.

- [7] Y. Seo and Z. J. Wang, 'Measurement and evaluation of specific absorption rate and temperature elevation caused by an artificial hip joint during mri scanning,' *Scientific Reports*, vol. 11, no. 1, p. 1134, 2021, ISSN: 2045-2322. DOI: 10.1038/s41598-020-80828-7. [Online]. Available: <https://doi.org/10.1038/s41598-020-80828-7>.
- [8] W. M. Brink, J. S. van den Brink and A. G. Webb, 'The effect of high-permittivity pads on specific absorption rate in radiofrequency-shimmed dual-transmit cardiovascular magnetic resonance at 3t,' *Journal of Cardiovascular Magnetic Resonance*, vol. 17, no. 1, p. 82, 2015, ISSN: 1532-429X. DOI: 10.1186/s12968-015-0188-z. [Online]. Available: <https://doi.org/10.1186/s12968-015-0188-z>.
- [9] Y. Ishihara, A. Calderon, H. Watanabe, K. Okamoto, Y. Suzuki, K. Kuroda and Y. Suzuki, 'A precise and fast temperature mapping using water proton chemical shift,' *Magn Reson Med*, vol. 34, no. 6, pp. 814–23, 1995, ISSN: 0740-3194 (Print) 0740-3194. DOI: 10.1002/mrm.1910340606.
- [10] V. Rieke and K. Butts Pauly, 'Mr thermometry,' *Journal of magnetic resonance imaging : JMRI*, vol. 27, no. 2, pp. 376–390, 2008, ISSN: 1053-1807 1522-2586. DOI: 10.1002/jmri.21265. [Online]. Available: <https://pubmed.ncbi.nlm.nih.gov/18219673%20https://www.ncbi.nlm.nih.gov/pmc/articles/PMC2780364/>.
- [11] P Wang, 'Evaluation of mr thermometry with proton resonance frequency method at 7t,' *Quantitative imaging in medicine and surgery*, vol. 7, no. 2, pp. 259–266, 2017, 28516051[pmid] PMC5418145[pmcid] qims-07-02-259[PII], ISSN: 2223-4292 2223-4306. DOI: 10.21037/qims.2017.03.05. [Online]. Available: <https://pubmed.ncbi.nlm.nih.gov/28516051%20https://www.ncbi.nlm.nih.gov/pmc/articles/PMC5418145/>.
- [12] N. W. Lutz and M. Bernard, 'Contactless thermometry by mri and mrs: Advanced methods for thermotherapy and biomaterials,' *iScience*, vol. 23, no. 10, pp. 101 561–101 561, 2020, 32954229[pmid] PMC7489251[pmcid] S2589-0042(20)30753-7[PII], ISSN: 2589-0042. DOI: 10.1016/j.isci.2020.101561. [Online]. Available: <https://pubmed.ncbi.nlm.nih.gov/32954229%20https://www.ncbi.nlm.nih.gov/pmc/articles/PMC7489251/>.
- [13] D. Bennett, 'Nacl doping and the conductivity of agar phantoms,' *Materials Science and Engineering: C*, vol. 31, no. 2, pp. 494–498, 2011, ISSN: 0928-4931. DOI: <https://doi.org/10.1016/j.msec.2010.08.018>. [Online]. Available: <https://www.sciencedirect.com/science/article/pii/S0928493110002110>.
- [14] Y. Chen, M. Ge, R. Ali, H. Jiang, X. Huang and B. Qiu, 'Quantitative mr thermometry based on phase-drift correction prf shift method at 0.35 t,' *BioMedical Engineering OnLine*, vol. 17, no. 1, p. 39, 2018, ISSN: 1475-

925X. DOI: 10.1186/s12938-018-0472-x. [Online]. Available: <https://doi.org/10.1186/s12938-018-0472-x>.

## Appendix A

# Additional Results

In Appendix A all the results that are not presented in Chapter 5 are displayed.

The raw temperature maps from Run 2 without any drift correction are presented in Figure A.1.

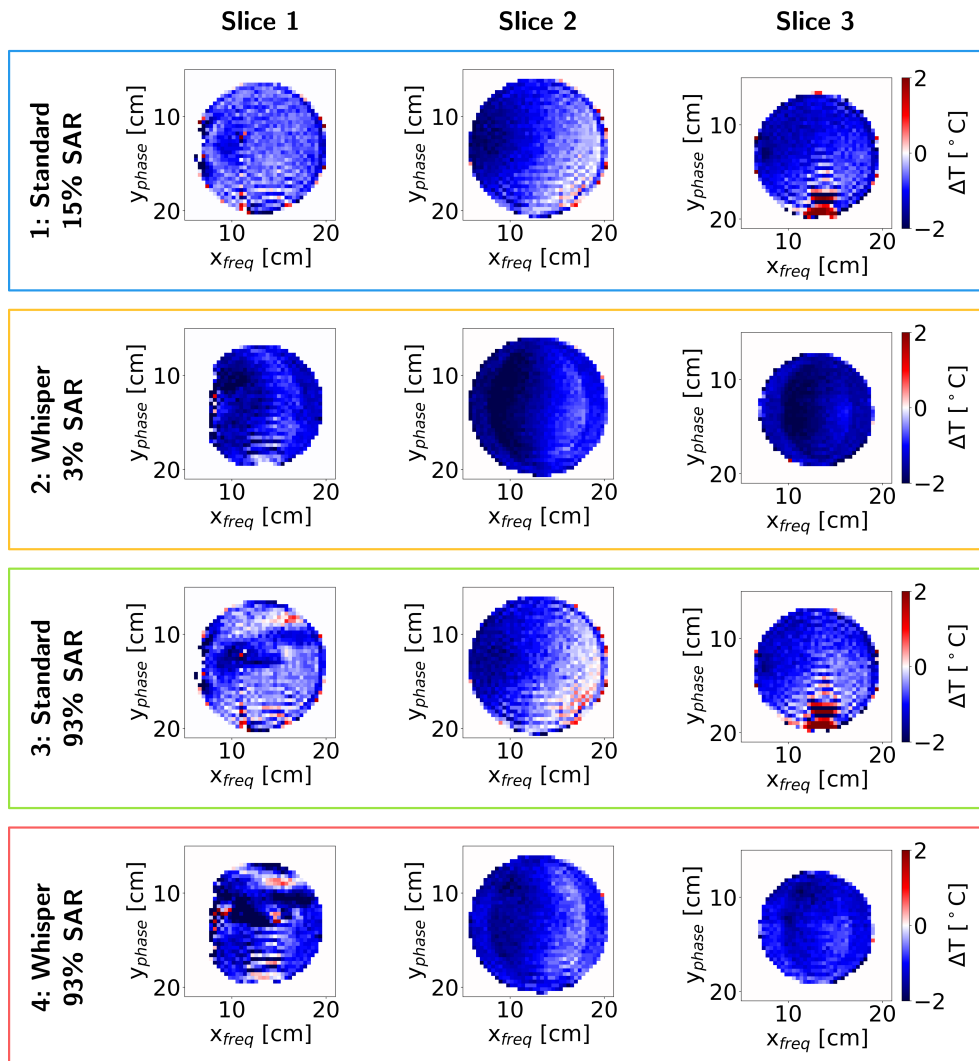


**Figure A.1:** Raw temperature maps from Run 2. The figure shows the last temperature map from all slices (1-3) and series (1-4). The last image shows the measured temperature change after acquiring the entire image series (10 minutes).

Figure A.2 shows the 0th order drift corrected temperature maps from Figure A.1.

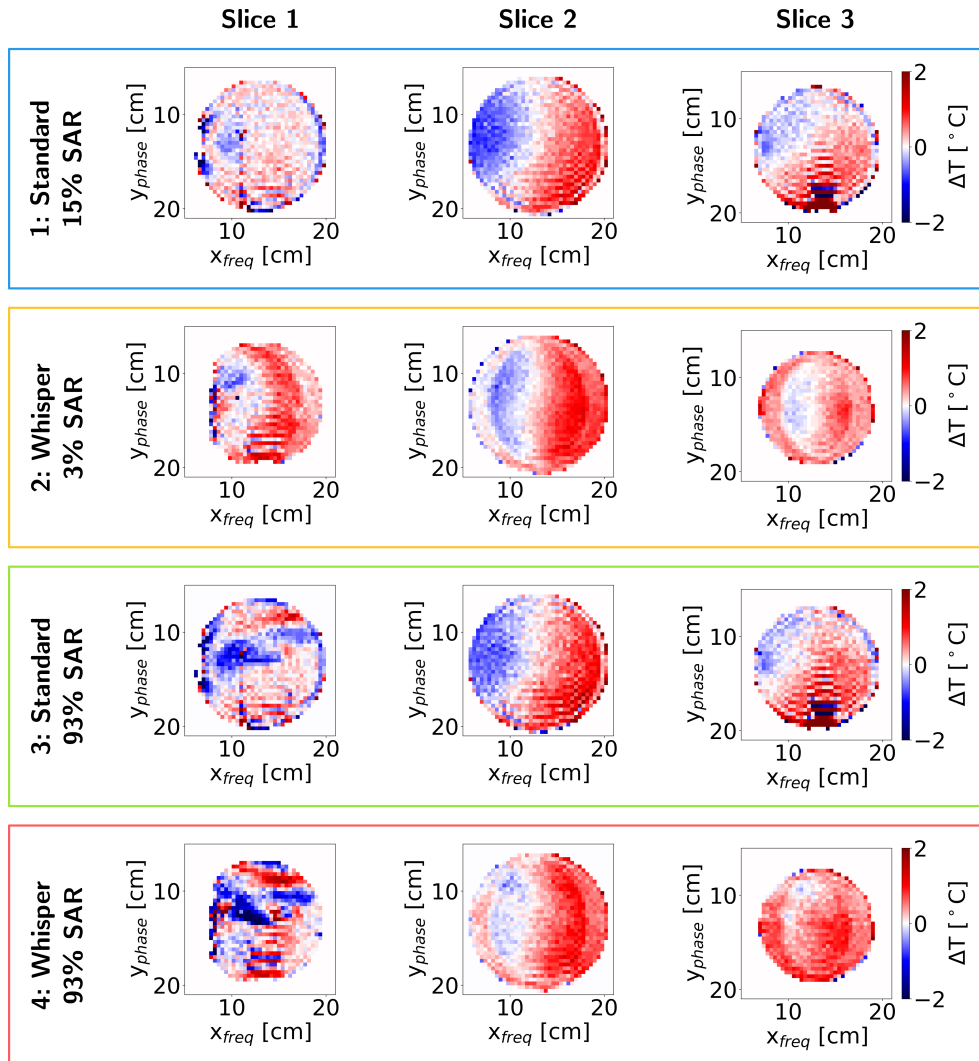


**Figure A.2:** 0th order drift corrected temperature maps from Run 2. The figure displays the last 0th order drift corrected temperature map from all slices (1-3) and series (1-4). The last image shows the measured temperature change after acquiring the entire image series (10 minutes).

The last temperature maps from the 0th and 1st order drift corrected Standard series from Run 2 are shown in Figure A.3.



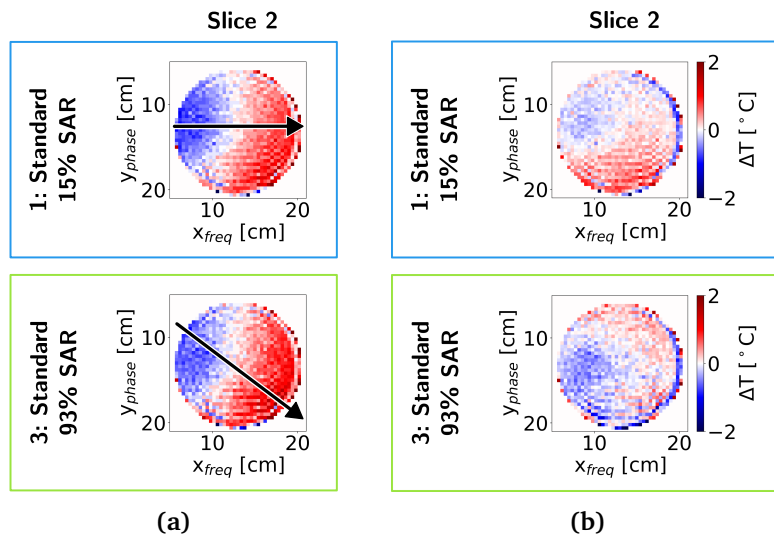


**Figure A.3:** (a) The last 0th order drift corrected images from Run 2. The arrow shows the estimated direction of the positive gradient in the 1st order spatial drift. (b) 0th and 1st order drift corrected images from Run 2. Only the images from slice 2 in the Standard series were corrected for both 0th and 1st order drift. This figure shows the last corrected temperature maps from slice 2 in the Standard series. The map shows the estimated temperature change after acquiring the entire image series (10 minutes).

## Appendix B

# Temperature Experiments

The temperature of the agar phantom placed in the MR scanner was recorded for 13.5 hours to observe the temperature evolution towards equilibrium. See Figure 5.1a for the temperature plot. The experiment showed that the temperature in the center of the phantom (Sensor A) stabilized at a temperature  $\approx 1^\circ\text{C}$  above temperature of the air surrounding the phantom (Sensor C). Sensor B was placed between the center and the edge of the phantom, and stabilized at  $\approx 0.5^\circ\text{C}$  above the air temperature. Physically it is not possible for the phantom to stabilize at a temperature above room temperature, nor maintaining a stable temperature gradient between sensor A and B.

A series of experiments were carried out to investigate the anomalous temperature readings. In Section B.1 the fiber optic sensors were tested to verify their accuracy. In Section B.2 the temperature evolution of a smaller sample of agar was measured to see if the gel itself affected the measurements.

### B.1 Fiber Optic Temperature Probe Validation

The aim of this experiment was to validate the Osensa fiber optic temperature probes (PRB-100-02M-STM-MRI). By setting up the temperature monitoring system similar to how it would be done for the scanning experiments, the temperature readings were evaluated both in air, water and with one probe's cable stretched out (as opposed to being coiled up). The latter was done to check if bending of the cable affected the readings. Water was chosen due to its stable and homogeneous temperature characteristics. The experiment showed that the temperature probes worked and yielded measurements within the stated accuracy of  $\pm 0.1^\circ\text{C}$ . The probes were likely not the reason for the strange offset between the temperature sensors in Figure 5.1a.

The data was recorded on a computer in the MR control room. The computer was connected by a USB cable to the transmitter (FTX-300-LUX+), also placed in the control room. The experiment was carried out in the MR scanning room. Extension cables (EXT-100-10M-STM-STM) going through the wall between the scanner and control room connected the probes to the transmitter. The probes

were connected to the extension cable by non-magnetic fiber couples (ACC-CON-STM-STM).

After setting up the experiment the data recording was started. The probes A, B and C were all placed in the air at the same position. When it was clear that the temperature readings were stable, the following actions were performed:

1. Probe A, B and C was placed in the water in a bottle.
2. Probe A, B and C was taken out of the water and back to original position in air.
3. Probe A's extension cable was stretched out, while the other remained coiled up. After stretching out the cable, the sensor head was placed back with sensor B and C again. Sensor A's cable was then stretched out, while B and C's cables were not.

The temperature data from the experiment are plotted in Figure B.1, where the dashed lines indicate the time points of the above events.

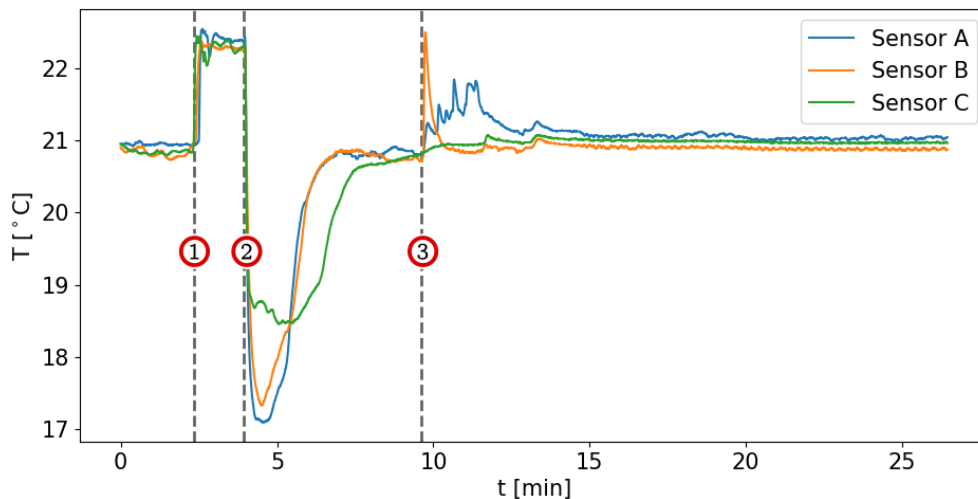


**Figure B.1:** Temperature probe test. In the beginning of the recording, all the sensors were placed at the same position in air. (1) After 2.5 min, all sensors were placed into water. (2) 4 min into the experiment all sensors were taken out again, back to their initial position. (3) Sensor A's cable was stretched out 9.6 min into the experiment.

At the start of the experiment, when the probes were placed in the air, the temperature values from all three probes were within the given accuracy of  $\pm 0.1^\circ\text{C}$  given by the data sheet. This was also the case after the probes were placed into water. When taken out of the water again, the temperatures dropped before rising towards equilibrium. This was due to the evaporation of water remaining on the sensors. Eventually, the data from all three probes were back within  $\pm 0.1^\circ\text{C}$ . Probe A's cable was then stretched out. Sensor B then showed a large spike in temperature, before quickly dropping down again to the air temperature. This could be due to being touched and handled. Sensor A also showed an increase in temperature

over  $\approx 4$  min. Stretching the cable took some time, and the temperature change most likely results from the probe being handled and moved around. After being placed back with the cable stretched out, the data again stabilized within  $\pm 0.1^\circ\text{C}$ .

The results from this experiment confirms that the temperature sensors work as expected. The temperature offset between the sensors in Figure 5.1a is likely not due to measurement error from the probes.

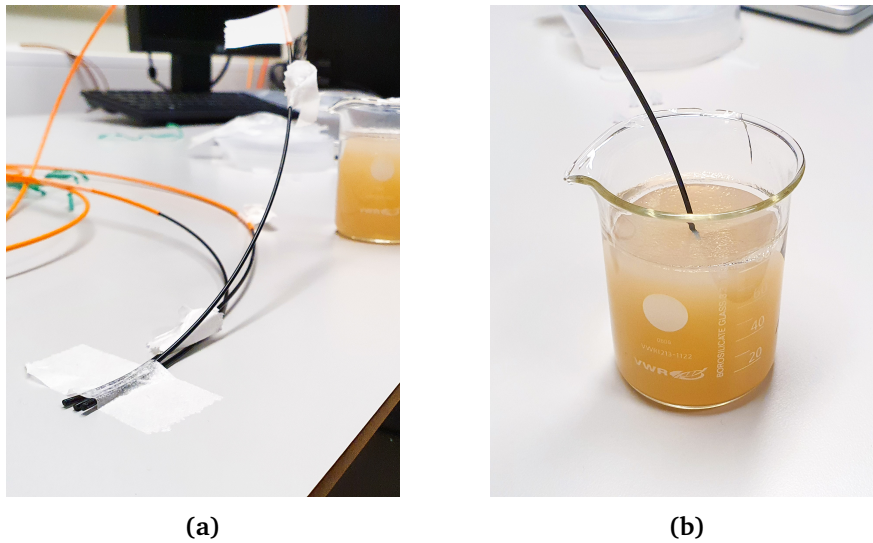
## B.2 Agar Temperature Experiment

The aim of this experiment was to evaluate if the offset in the temperature readings in Figure 5.1a were due to the agar gel interacting with the temperature probes. To do so, a small beaker filled with the same agar solution as in the custom phantom was used for temperature measurements. One can not conclude from this experiment that the gel does not affect the temperature readings.

This experiment was performed in the MR control room. The data was logged at a computer connected by USB cable to the transmitter. The fiber optic temperature probes (PRB-100-02M-STM-MRI) were connected directly to the transmitter. The experiment was performed in the following way:

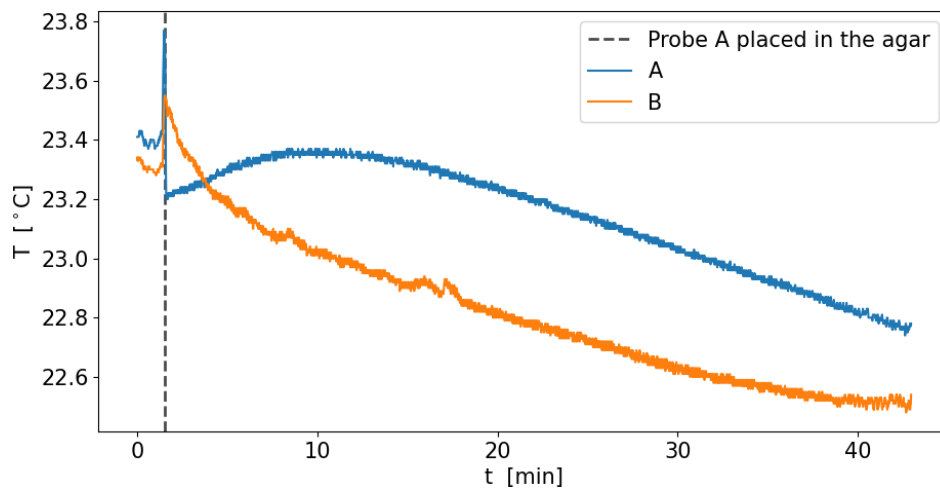
1. The beaker filled with agar gel was kept in the control room for several days before the experiment to reach thermal equilibrium.
2. The temperature probes were set up as described above, and taped to the table. See Figure B.2a. The recording was then started.
3. After 1.5 min, when the temperature data seemed stable, probe A was placed in the agar gel. See Figure B.2b.
4. After probe A was placed in the Agar, the temperature was logged for about 40 min.

Figure B.2 shows pictures of the temperature probes and the beaker with the agar gel.



**Figure B.2:** Agar temperature experiment setup. (a) At the start of the experiment, all probes were taped to the table. Note that probe A, B, and C are in the image, but only data from A, and B was logged. (b) The agar gel with probe A placed in it.

The temperature data from the experiment is plotted in Figure B.3.



**Figure B.3:** Temperature plot from agar gel experiment.

At the start of the recording, the temperature data from probe A and B were within the  $\pm 0.1^\circ\text{C}$  accuracy of the probes. When probe A was placed in the agar, the temperature from probe B jumped by  $\approx 0.2^\circ\text{C}$ , most likely due to being handled by a warm hand when moving probe A. The temperature data from probe B, still placed in the air, then started declining. From the plot in Figure B.3, probe B's temperature seemed to stabilize at  $22.5^\circ\text{C}$ , which was  $0.8^\circ\text{C}$  lower than the tem-

perature at the start of the experiment. This temperature change could be due to the ventilation system or some other factors.

When placed in the agar gel, the temperature readings dropped 0.2°C, indicating that the agar gel was slightly cooler than the air temperature. The temperature then seemed to rise for about 10 min, before decreasing again. The reason for this is unclear. The recording of temperature data was not done for a long enough duration to see if the agar temperature would stabilize at the same temperature as the air.

The results from this experiment were unclear and did not provide any definite answers to whether or not the agar gel affects the temperature readings. More experiments should be performed.

# Appendix C

## Code

In Appendix C the most important functions from the temperature map processing in Python is shown. For the full code go to <https://github.com/cfhaakonsen/master>. For access to the repository, please contact the author at [cfhaakonsen@gmail.com](mailto:cfhaakonsen@gmail.com).

The sequence code can not be shared due to Siemens confidentiality.

### C.1 Temperature Map Formation

Listing C.1 shows the function converting the phase images to temperature maps.

**Code listing C.1:** Function converting the phase images to temperature maps.

```
1
2 def phase_to_temp(ses_dict: dict) -> dict:
3     """
4     Converts the phase values to temperature change, and adds the temperature change images
5     to the dictionary. The first image is used as reference, and the temperature change values
6     are relative to the temperature in this image. Complex subtraction is used instead of just
7     simply subtracting the phases.
8
9     :param ses_dict:
10    :return:
11    """
12
13    # Declaring parameters
14    alpha = -0.01 * 1e-6 # - 0.01 ppm
15    gamma = 2.675 * 1e8 # 2.675 rad/s/T
16    B0 = 7.0 # 7 T
17    delta_TE = 1.02 * 1e-3 # 1.02 ms
18
19    # Phase images that will be converted into temperature change images
20    images = ses_dict['PhaseImages']
21    test_images = ses_dict['PhaseImages']
22
23    # Making nparray for containing temperature images
24    temp_images = np.zeros_like(images)
25
26    # Making the phase values complex for complex subtraction of the phases. May avoid wrapping issues.
27    images = np.exp(1j * images)
28
```

```

29 # Calculating the temperature maps for each slice
30 for i in range(ses_dict['NumSlices']):
31
32     # Conjugating the first image from the slice, which is used as reference
33     reference = np.conj(images[:, :, i, 0])
34
35     # Looping through all the images from that slice
36     for j in range(images.shape[3]):
37
38         # Calculating the phase difference
39         phase_diff = np.angle(reference * images[:, :, i, j])
40
41         # Converting to temperature change
42         temp_image = phase_diff / (alpha * gamma * B0 * delta_TE)
43
44         temp_images[:, :, i, j] = temp_image
45
46 # Adding the temperature change maps to the dictionary
47 ses_dict['TempImages'] = temp_images
48
49 return ses_dict

```

## C.2 0th Order Drift Correction

Listing C.2 shows the function removing the 0th order drift.

**Code listing C.2:** Implementation of 0th order drift correction.

```

1
2 def zeroth_order_correction(ses_dict: dict, temp_path: str, sensor_num=1, center=(31, 25),
3                             radius=None, show_mask=False) -> dict:
4     """
5
6     :param ses_dict: Dictionary containing all the series data
7     :param temp_path: Path to temperature probe data
8     :param sensor_num: A=1, B=2 C=3
9     :param center: Coordinates of the center where drift correction
10    is performed.
11    :param radius: Radius of ROI in pixels.
12    :return:
13    """
14
15    # Loading the Osensa temperature data
16    temp_data = dataload.load_temperature_data(temp_path)
17
18    # Getting start and stop time for gating the temperature data
19    start, stop = utils.series_start_stop_time(ses_dict)
20
21    # Time gating the data
22    temp_data = utils.time_gate_temp_data(temp_data, start, stop)
23
24    # Extract the sensor from one sensor only and converting to
25    # temperature change from absolute temperature
26    temp_data = temp_data[:, [0, sensor_num]]
27    temp_data[:, 1] = temp_data[:, 1] - temp_data[0, 1]

```



```

28
29 # Making a copy of the temperature images for the corrected image
30 temp_images = ses_dict.get('TempImages')
31 corrected_temp_images = temp_images.copy()
32
33 # Getting the masks
34 masks = ses_dict['Masks']
35 masks = np.expand_dims(masks, len(masks.shape))
36
37 for slice in range(3):
38
39     # Getting the mean temperature values from the ROI
40     means, _ = statistics.circular_mask_mean_std(
41         ses_dict, slice=slice, center=center, radius=radius, show_mask=show_mask)
42
43     # Getting the image times
44     image_times = ses_dict['ImageTimes'][slice, :]
45
46     # Subtracting first value to get delta time
47     delta_time = image_times - image_times[0]
48
49     # Converting the temp_data to float64 from object. Necessary for interpolation
50     temp_data = temp_data.astype('float64')
51
52     # Interpolating the sensor data to the PRF sample axis
53     interp_temp_data = np.interp(image_times, temp_data[:, 0], temp_data[:, 1])
54
55     # Calculating the error between the PRF thermometry data and the probe data
56     temp_error = means - interp_temp_data
57
58     # Performing linear regression on the error to find an estimate for the zeroth order drift
59     model = LinearRegression().fit(delta_time.reshape(-1, 1), temp_error)
60
61     y_pred = model.predict(delta_time.reshape(-1, 1))
62
63     # Removing the estimated zeroth order drift from the images
64     corrected_temp_images[:, :, slice, :] = (
65         (corrected_temp_images[:, :, slice, :] - y_pred) * masks[:, :, slice, :]
66     )
67
68
69 ses_dict['CorrectedTempImages'] = corrected_temp_images
70
71 return ses_dict

```

### C.3 1st Order Drift Correction

Listing C.3 shows the function removing first order drift. Some parts of the drift correction was put in separate functions, which are presented after.

**Code listing C.3:** Implementation of 1st order drift correction.

```

1
2 def first_order_drift_correction(ses_dict: dict, probe_center=None, slice=1) -> dict:

```

```

3     '''
4     Performes first order drift correction on the center slice.
5
6     :param ses_dict: Dictionary containing all the data from the series
7     :return: Returns updated series dictionary
8     '''
9
10    # Getting the dimensions of the image
11    h, w = ses_dict['TempImages'].shape[0], ses_dict['TempImages'].shape[1]
12
13    # Using the center of the image as mask center if not provided
14    if probe_center is None:
15        probe_center = (int(h / 2), int(w / 2))
16
17    # Estimating the angle of the positive gradient relative to the positive y-axis
18    angle = estimate_gradient_angle(ses_dict, slice=slice, show_plots=False)
19
20    # Predicitng the slopes of the first order drift
21    pred_drift_slope = estimate_gradient_slope_evolution(ses_dict, angle, slice=slice, show_plots=False)
22
23    # Getting the images
24    images = ses_dict['CorrectedTempImages'][:, :, slice, :]
25
26    plot_num = 76 # Use 70 for all figures except the subtraction figure
27
28    for image_num in range(images.shape[2]):
29
30        # Making the gradient image that will be subtracted
31        grad_image = make_gradient_image(
32            ses_dict, slope=pred_drift_slope[image_num], image_dim=None
33        )
34
35        grad_image = rotate_gradient_image(grad_image, angle=-angle) # Rotates counter clockwise!
36
37        # Shifting the gradient image to fit with the temperature probe
38        # shift = [probe_center[0] - int(h/2), probe_center[1] - int(w/2)]
39        shift = [probe_center[1] - int(h / 2), probe_center[0] - int(w / 2)]
40        grad_image = ndimage.shift(grad_image, shift)
41
42        # Masking the gradient image
43        grad_image = grad_image * ses_dict['Masks'][:, :, 1]
44
45
46        images[:, :, image_num] = images[:, :, image_num] - grad_image
47
48
49    return ses_dict

```

Listing C.4 shows the function that estimates the angle of the gradient due to 1st order drift.

**Code listing C.4:** Function estimating the 1st order drift gradient angle.

```

1
2 def estimate_gradient_angle(ses_dict: dict, slice=1, show_plots=False) -> int:
3     """
4     Estimates the angle of the gradient relative to the positive y-axis.

```

```

5
6     :param ses_dict:
7     :return:
8     """
9
10    # Using the mean of the last ten images to estimate the gradient angle. Goal to reduce impact of noise.
11    image = np.mean(ses_dict['CorrectedTempImages'][:, :, slice, -10:], axis=2)
12
13    # Plotting the mean image
14    if show_plots:
15        save_path = r"C:\Users\cfhaa\OneDrive_\NTNU\Master\Figurer\Metode\1stcorrection\meanImage.png"
16        utils.plot_temp_map(ses_dict, image, savepath=save_path)
17
18    # Calculating the projection for each angle
19    thetas = np.linspace(0, 180, 180, endpoint=False)
20
21    # Making the sinogram
22    sinogram = radon(image, theta=thetas)
23
24    # Cropping the sinogram
25    cropped_sinogram = sinogram[14:49, :]
26
27    # Making an axis for the linear regression
28    axis = np.linspace(0, cropped_sinogram.shape[0], cropped_sinogram.shape[0], endpoint=False)
29    axis = axis.reshape(-1, 1)
30
31    # Values for keeping the maximum slope and corresponding angle
32    max_angle = 0
33    max_slope = 0
34
35    for angle in range(cropped_sinogram.shape[1]):
36
37        # Performing linear regression on the error to find an estimate for the zeroth order drift
38        model = LinearRegression().fit(axis, cropped_sinogram[:, angle])
39
40        # Getting the slope after the linear regression
41        slope = model.coef_[0]
42
43        # Updating the max slope and its angle if it is the largest
44        if abs(slope) > abs(max_slope):
45            max_slope = slope
46            max_angle = angle
47
48    # The max_angle is the angle perpendicular to the gradient relative to the negative y-axis.
49    # Converting to the angle of the positive gradient relative to the positive y-axis.
50    if max_slope >= 0:
51        angle = 180 - max_angle + 90 + 180
52    else:
53        angle = 180 - max_angle + 90
54
55    return angle

```

Listing C.5 shows the function estimating the evolution of the 1st order drift gradient slope.

**Code listing C.5:** Function estimating the 1st order gradient slope evolution.

```

1
2 def estimate_gradient_slope_evolution(ses_dict: dict, angle: int, slice=1, show_plots=False):
3
4     # Not including the first image as that should be zero. Could be removed earlier.
5     images = ses_dict['CorrectedTempImages'][:, :, slice, 1:]
6
7     # Getting the mask and rotating it the same amount as the images will be
8     mask = ses_dict['Masks'][:, :, slice]
9     rotated_mask = ndimage.rotate(mask, angle, reshape=False)
10
11    # List for containing slope values
12    slope_values = []
13
14    # Looping through all the images
15    for image_num in range(images.shape[2]):
16
17        # Getting the image
18        image = images[:, :, image_num]
19
20        # Rotating the image
21        image = ndimage.rotate(image, angle, reshape=False)
22
23        # Calculating the mean along the x-axis including only values within the mask
24        # I expect to see RuntimeWarnings in this block
25        with warnings.catch_warnings():
26            warnings.simplefilter("ignore", category=RuntimeWarning)
27            grad_mean = np.mean(image, axis=1, where=rotated_mask)
28
29        # Cropping away empty values + around 1 pixel
30        grad_mean = grad_mean[13:47]
31
32        # Making an axis for the linear model
33        axis = np.linspace(0, grad_mean.shape[0], grad_mean.shape[0], endpoint=False)
34        axis = axis.reshape(-1, 1)
35
36        # Estimating the slope
37        model = LinearRegression().fit(axis, grad_mean)
38
39        # Getting the slope value
40        slope = model.coef_[0]
41
42        # Adding the value to the list
43        slope_values = np.append(slope_values, abs(slope))
44
45
46    # Predicting the slope evolution by linear regression
47    # Making an axis for the linear model
48    axis = np.linspace(0, slope_values.shape[0], slope_values.shape[0], endpoint=False)
49    axis = axis.reshape(-1, 1)
50
51    # Fitting a linear regression model
52    model = LinearRegression().fit(axis, slope_values)
53
54    # Predicting the slope evolution
55    pred_drift_slope = model.predict(axis)
56
57    # Adding zero as first value so the array fits the number of images
58    pred_drift_slope = np.append([0], pred_drift_slope)
59
60    return pred_drift_slope

```

Listing C.6 shows the function making a gradient image, which was used for subtraction of 1st order drift.

**Code listing C.6:** Function making the gradient image used to subtract 1st order drift.

```

1
2 def make_gradient_image(ses_dict: dict, slope: float, image_dim=None):
3
4     if image_dim is None:
5         image_dim = ses_dict['TempImages'][:, :, 0, 0].shape[0]
6
7     # Making the axis centered around 0
8     gradient = np.linspace(0, image_dim-1, image_dim)
9     gradient = gradient - image_dim/2 + 0.5
10
11    # Multiplying with -1 so that the gradient is increases along the y-axis
12    gradient = gradient * -1
13
14    # Multiplying with the slope to make the gradient
15    gradient = gradient * slope
16    gradient = np.expand_dims(gradient, axis=1)
17
18    gradient_image = np.tile(gradient, (1, image_dim))
19
20    return gradient_image

```

Listing C.7 shows the function used for rotating the made gradient image.

**Code listing C.7:** Function rotating the gradient image used to subtract 1st order drift.

```

1
2 def rotate_gradient_image(gradient_image, angle=0, pivot_point=(32, 32), show_image=False):
3
4     # Padding the image to double size so that the pivot point is in the image center
5     pad_x = [gradient_image.shape[1] - pivot_point[0], pivot_point[0]]
6     pad_y = [gradient_image.shape[0] - pivot_point[1], pivot_point[1]]
7
8     # Padding the image
9     gradient_image = np.pad(gradient_image, [pad_y, pad_x], 'constant')
10
11    # Rotating the image
12    gradient_image = ndimage.rotate(gradient_image, angle, reshape=False)
13
14    # Cropping the image back to its original dimensions
15    gradient_image = gradient_image[pad_y[0]:-pad_y[1], pad_x[0]:-pad_x[1]]
16
17    if show_image:
18        plt.imshow(gradient_image, cmap='seismic', vmax=2, vmin=-2)
19        plt.show()
20
21    return gradient_image

```